Assessing Thermal Response of Redox Conduction for *Anti*-Arrhenius Kinetics in a Microbial Cytochrome Nanowire

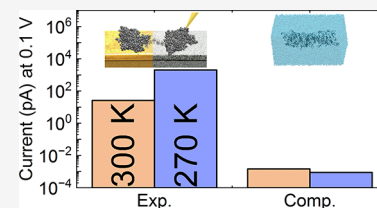Matthew J. Guberman-Pfeffer*

ACCESS | Metrics & More | Article Recommendations | SI Supporting Information

ABSTRACT: A micrometers-long helical homopolymer of the outer-membrane cytochrome type S (OmcS) from *Geobacter sulfurreducens* is proposed to transport electrons to extracellular acceptors in an ancient respiratory strategy of biogeochemical and technological significance. OmcS surprisingly exhibits higher conductivity upon cooling (*anti*-Arrhenius kinetics), an effect previously attributed to H-bond restructuring and heme redox potential shifts. Herein, the temperature sensitivity of redox conductivity is more thoroughly examined with conventional and constant-redox and -pH molecular dynamics and quantum mechanics/molecular mechanics. A 30 K drop in temperature constituted a weak perturbation to electron transfer energetics, changing electronic couplings ($\langle H_{mn} \rangle$), reaction free energies (ΔG_{mn}), reorganization energies (λ_{mn}), and activation energies (E_a) by at most $|0.002|$, $|0.050|$, $|0.120|$, and $|0.045|$ eV, respectively. Changes in ΔG_{mn} reflected -0.07 ± 0.03 V shifts in redox potentials that were caused in roughly equal measure by altered electrostatic interactions with the solvent and protein. Changes in intraprotein H-bonding reproduced the earlier observations. Single-particle diffusion and multiparticle steady-state flux models, parametrized with Marcus theory rates, showed that biologically relevant incoherent hopping cannot qualitatively or quantitatively describe electrical conductivity measured by atomic force microscopy in filamentous OmcS. The discrepancy is attributed to differences between solution-phase simulations and solid-state measurements and the need to model intra- and intermolecular vibrations explicitly.

The graphic shows Current (pA) at 0.1 V on the y-axis ranging from 10^{-4} to 10^6, with bars labeled 300 K and 270 K under "Exp." and "Comp."

1. INTRODUCTION

All respiratory life is powered by the flow of electrons through a chain of reduction−oxidation (redox)-active cofactors.[1,2] Electrons enter the chain by oxidation of a primary donor (e.g., organic matter) and exit via reduction of a terminal acceptor (e.g., O_2),[3] both of which are ordinarily internalized by a cell. The nearest electron donor/acceptor in some aquatic sediments, however, is either another microbe or a mineral nanoparticle that may be up to a few microns away. Coupling the reduction of microbes or minerals in the extracellular space with intracellular oxidative metabolism constitutes an ancient and widespread respiratory strategy.[4−7] The electrical circuits established between microbes and minerals, if better understood, can elucidate the biogeochemical evolution of the planet,[8−13] the role of the microbiome in human health and diseases,[14−17] as well as templates[18−21] for the design of bioelectronic technologies.[21−34]

Microbes can electrically "plug-in" to their environments through direct contact with cell-surface proteins, outer-membrane vesicles, filamentous appendages, or molecular shuttles. One of the best studied electroactive microorganisms, *Geobacter sulfurreducens*, discharges ~10^5 electrons/s/cell.[35] This fA current has been known for nearly 20 years to be carried by conductive filaments,[36] but questions about the identity, composition, and conductivity mechanism of the filaments have[37−42] and continue[43−55] to be debated.

Homopolymers of a mostly α-helical pilin protein[47,52] or outer-membrane multiheme cytochromes[46,56] have been proposed as "nanowires" used by *G. sulfurreducens*. The pilin-based polymer, called a pilus, was hypothesized to transport electrons through a continuous chain of stacked aromatic residues (Figure 1, *top left*) by either multistep charge hopping or bandlike charge transport.[57−69] However, a recently reported cryogenic electron microscopy (CryoEM) structure differed markedly from the proposed model (Figure 1, *top middle* vs *top left*) and had a conductivity 10^4 times smaller than what was previously attributed to the pilus.[51] The electrically conductive or *e*-pili have been suggested to not exist as such,[46,51] being instead the misidentified filamentous outer-membrane cytochrome type S (OmcS) (Figure 1, *top right*).[46]

OmcS was revealed by CryoEM[46] to feature a spiraling chain of bis-histidine-ligated *c*-type heme cofactors encased within a protein sheath. The structure is analogous to a man-made electrical wire if the protein is assumed (perhaps oversimplistically) to provide only insolation for the conductive heme chain. Questions concerning the physiological relevance of this structure are actively being investigated.[53] An equally important question receiving much less attention is whether
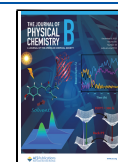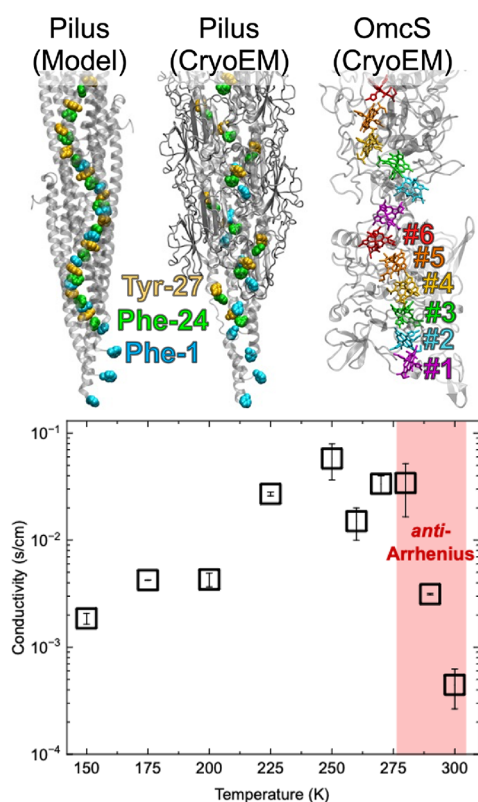
Figure 1. (*Top*) Structures of the (*left*) hypothetical *G. sulfurreducens* pilus from ref 63, (*middle*) CryoEM structure of the pilus from ref 51, and (*right*) CryoEM structure of the outer-membrane cytochrome type S (OmcS) filament from ref 46 that is the subject of the present study. (*Bottom*) Temperature-dependent electrical conductivity of OmcS filaments. The data are reproduced from Figure 4A in ref 80.

electrical characterizations of OmcS by atomic force microscopy (AFM) report on the same charge transport mechanism that operates under biological conditions.[70−73] There are currently large discrepancies separating expectations, theories, and experiments for the charge transport mechanism in OmcS.

Similar to other chains of redox-active cofactors in photosynthesis and respiration, electrons are expected to move in a "bucket-brigade"-like series of redox reactions along the heme chain in OmcS.[72,74,75] The kinetics of each step are usually well described by the nonadiabatic Marcus theory.[76,77] In this framework, electron transfer results from thermal fluctuations that bring the reactant and product states into energetic degeneracy. Such fluctuations are rare events, and become more so at lower temperatures (Arrhenius-type kinetics), because the activation barriers are large, and the transition state regions are cusped because of weak electronic interactions between adjacent hemes.[78] In between the nonadiabatic "hops" from reactant to product states, the electrons reside long enough on each heme to lose coherence as the nuclei respond to the change in charge state. Biological redox conduction is multistep incoherent hopping.[74]

Theoretical studies suggest that this mechanistic picture is consistent with the CryoEM structure but not the AFM-measured conductivity at 300 K for OmcS. For example, activation energies and electronic couplings computed from the CryoEM structure were found (and confirmed herein) to be ≥0.1 and ≤0.01 eV, respectively.[79,80] Conductivities computed with these energetic values for incoherent heme-

to-heme hopping, however, severely underestimated the AFM-measured value,[81] a discrepancy sometimes only admitted by the omission of a direct comparison.[80] If the hops were assumed to occur instead between nanometer-sized blocks of coherently coupled hemes, the predicted conductivity was able to approach the experimental value.[81] However, it is unclear how a protein with 81% turns and loops comprising the secondary structure[46] can be sufficiently rigid to preserve coherence among as many as two dozen hemes when the electronic coupling between any pair is less than thermal energy.[79−81] Furthermore, decoherent quantum transport was found to be capable of explaining as much as 71% of the measured conductance.[82]

Thermally activated hopping also seems at odds with the AFM-measured temperature dependence of electrical conductivity in OmcS (Figure 1, *bottom*). Instead of decreasing upon cooling as expected, the conductivity increased by a factor of 10^2 from 300 to 270 K.[80] To reconcile redox conduction with this *anti*-Arrhenius kinetics, a "massive restructuring" of intraprotein H-bonds upon cooling was computationally proposed to modulate heme redox potentials and, in turn, the activation energies for incoherent heme-to-heme charge transfer.[80] Below 250 K, the conductivity generally decreased, but confusingly, the conductivity remained at least 10 times larger than what it was at 300 K.[80]

Since the present author contributed to the structural transition proposal for *anti*-Arrhenius kinetics, several observations have suggested the explanation to be an artifact of unphysical energetic parameters. These observations include the following: (1) One of the hemes was predicted to have a redox potential >0.15 V more negative than expected experimentally for a bis-histidine-ligated c-type heme (−0.521 V vs standard hydrogen electrode (SHE)).[83] The potential was also >0.4 V, half the known biological range for heme cofactors in general,[83] more negative than the adjacent heme in van der Waals contact. The resulting large free energy differences to/from this heme may have caused an under-estimation of the computed conductivity at 310 K, thereby causing the conductivity at 270 K to appear larger by comparison. (2) Although temperature-induced shifts in redox potentials for cytochromes are known,[84−91] the computed shifts were unexpectedly large and of mixed sign (e.g., −0.189 and +0.113 V) for hemes in van der Waals contact.[80] (3) A global descriptor was invoked to characterize the cooling-induced restructuring of the H-bonding network, but it could not explain the distinct temperature dependencies of the six hemes in a subunit of the filament. Only weak ($R^2 \approx$ 0.6) correlations were found with other factors like heme macrocycle nonplanarity and electric field strength on the Fe centers.

If these misgivings are warranted, then there is no theoretical description yet available that satisfactorily links the CryoEM structural and AFM electrical characterizations of OmcS, and the latter may reflect mechanism(s) distinct from what operates in the biological context. If the misgivings are not supported by a closer examination, then there is still some deficiency in current models because redox conduction fits qualitatively but not quantitatively with the AFM measurements. Either way, a more thorough assessment of temperature-dependent redox conduction is needed—and provided herein—to identify next steps for refining structure−function relationships in microbial cytochrome "nanowires". The urgency in addressing the gaps between biological expect-

ations, theoretical models, and AFM measurements on charge transport is underscored by the expanding library of filamentous cytochromes, one of which is 10^3 times more conductive than OmcS.[46,56,92,93] The mechanistic knowledge is also a prerequisite for re-engineering these structures for sustainable bioelectronic technologies. These considerations motivated the present study.

Using >7 μs of conventional and constant-redox and -pH (C(E,pH)) molecular dynamics (MD), as well as quantum mechanics/molecular mechanics (QM/MM) computations on >3000 configurations, redox potentials and temperature coefficients were found in much better agreement with experimental expectations than in the prior work.[80] Biologically relevant redox conduction based on these new potentials, using both single-particle diffusion and multiparticle steady-state flux kinetic schemes, failed to explain AFM electrical measurements either quantitatively or qualitatively as a function of temperature. Taking into account differences between solution-phase simulations and solid-state measurements, (1) computation of electron transfer reorganization energies to model the dehydration of the filament in AFM experiments improved quantitative agreement with the measured conductivity, and (2) QM/MM computations with explicit and implicit aqueous solvents indicated that 60% of the cooling-induced shifts on redox potentials result from the microstructure of the solvent. These observations point to a hitherto unappreciated dependence of the electrical properties in cytochrome "nanowires" on the physical conditions of the experiments.

2. METHODS AND COMPUTATIONAL DETAILS

An overview of the computational workflow is shown in Figure 2, with extensive details reserved for the Supporting
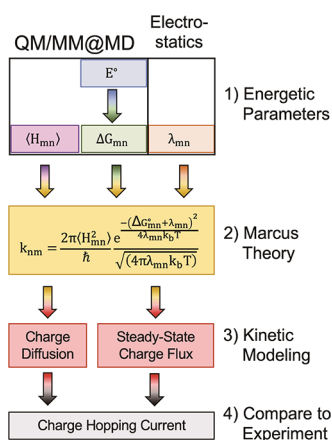
Figure 2. High-level overview of the computational workflow employed in the present study. See the SI for methodological details. QM/MM@MD = quantum mechanics/molecular mechanics at molecular dynamics generated configurations. E° = redox potential; $\langle H_{mn} \rangle$ = electronic coupling; ΔG_{mn} = reaction free energy; λ_{mn} = reorganization energy.

Information (SI). Briefly, the dynamics of a three-subunit OmcS filament were simulated in fully oxidized and single-heme-reduced microstates by conventional MD or as a function of solution potential with constant-redox (CE) MD (SI Section S1.2). Redox potentials (E°'s), and by extension reaction free energies (ΔG_{mn}'s; m = donor, n = acceptor) (SI Section S1.3.2), electronic couplings ($\langle H_{mn} \rangle$'s, SI Section S1.3.3), and reorganization energies (λ_{mn}'s, SI Section S1.4),
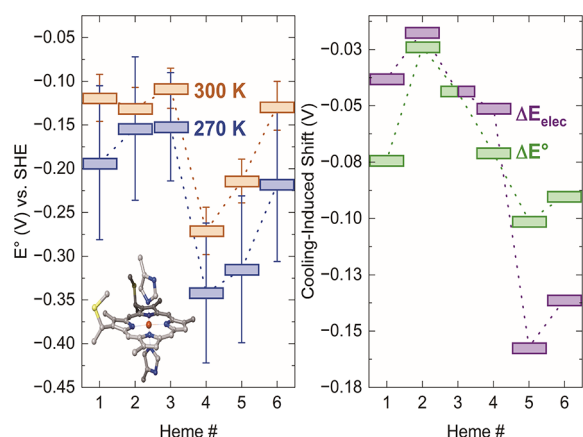
were then computed with either classical electrostatics or quantum mechanics/molecular mechanics at molecular dynamics-generated configurations (QM/MM@MD). These energetic terms were used to compute Marcus theory rates for heme-to-heme electron transfers (SI Section S1.5), which in turn parameterized single-particle diffusion (SI Section 1.6.1) and multiparticle steady-state flux (SI Section 1.6.2.) kinetic schemes. The obtained diffusion constant or charge flux was related to an electrical current (SI Section S1.6) for direct comparison to AFM experiments. Additional simulations and analyses were performed to characterize the temperature dependence of intraprotein H-bonding between 100 and 400 K (SI Section S1.7) and the change in density of solvation shells upon cooling (SI Section 1.8). The extent of charge compensation coupled to reduction of the hemes was assessed by computing pK_as with constant pH molecular dynamics (CpHMD) for different redox microstates and applying the Henderson–Hasselbalch equation.

3. RESULTS AND DISCUSSION

Heme redox potentials (E°'s) at 300 and 270 K are first analyzed. These temperatures bracket the range for *anti*-Arrhenius behavior in electrical conductivity (Figure 1, *bottom*). The cooling-induced shifts in redox potential (ΔE°) are interpreted in terms of altered electrostatic interactions with the protein and solvent, where the microstructure of the solvent is found to play a particularly important role. The previously postulated role of restructured intraprotein H-bonds[80] is also examined. The temperature dependence of the free energy landscape for heme-to-heme charge transfer, defined by the computed E°'s, is then discussed. Finally, redox conductivity and its temperature dependence are analyzed with multiple kinetic schemes. Because no theoretical model to date, including the present study, successfully explains the temperature dependence of electrical conductivity in filamentous OmcS, the discussion ends with a survey of possible mechanisms invoked to explain *anti*-Arrhenius kinetics in other systems.

3.1. Temperature Dependence of Heme Redox Potentials. *3.1.1. High (300 or 310 K) Temperature.* E°'s at 300 K for the hemes in filamentous OmcS were −0.063 to −0.271 V vs SHE according to QM/MM@MD computations (Figure 3, *left*; Tables S3 and S11). Use of a triple- instead of double-ζ basis set shifted the values toward the positive end of the range by 0.034 ± 0.013 (mean ± standard deviation) V, a magnitude comparable to the standard error of the mean for each E° (Figure S2; Tables S2, S3, and S11). The range for E° at 300 K was likewise −0.093 to −0.306 V vs SHE according to C(E,pH)MD simulations (Figure S6; Table S10). These ranges were consistent with the experimental range of +0.150 to −0.350 V vs SHE reported for bis-histidine-ligated *c*-type hemes.[83] Thus, the computed E°'s were converged with respect to basis set quality, consistent at multiple levels of theory, and in good agreement with experimental expectations. Results presented below were obtained with the double-ζ basis set unless otherwise noted.

Along the linear heme chain from #1 → #2 ... #6 in filamentous OmcS (and the x axis in Figure 3, *left*), the E°'s at 300 K fluctuated within |0.022| V from #1 to #3, plummeted by −0.163 V from #3 to #4, and recovered to within 0.025 V (thermal energy at 290 K for a one-electron process) of the starting E° from #4 to #6.

Figure 3. Cooling-induced shifts in heme redox potentials and a correlation with altered Coulombic interactions. (*Left*) Redox potentials at 300 and 270 K computed with quantum mechanics/molecular mechanics at molecular dynamics-generated configurations (QM/MM@MD) using B3LYP/[Fe = LANL2DZ; H, C, N, S = 6-31G(d)]:AMBER99SB. The QM region is shown in the inset. (*Right*) Correlation between cooling-induced shifts in redox potential and electrostatic energies for heme oxidation.

From the viewpoint of the electron transport function of filamentous OmcS, it is striking that the protein tunes the $E°$'s of six chemically identical heme groups over ~0.2 V and yet arranges the hemes so that there is no net change in $E°$ through a subunit of the filament. A similar "design" strategy was found for the deca-heme protein MtrF from *Shewanella oneidensis*.[94] The strategy is also consistent with the need for long-range charge transport through a homopolymer, perhaps supporting the physiological relevance of filamentous OmcS. The mechanisms regulating the redox profile of OmcS are delineated in a manuscript under preparation.

$C(E,pH)$MD simulations captured much of the same behavior for $E°$ along the heme chain as QM/MM@MD (Figure S6), except that (1) the swings in $E°$ were more accentuated, as is expected for a fix-point charge electrostatics method,[95] and (2) the $E°$ of #6 was more, not less, negative than #5. The latter discrepancy may reflect the difficulty of assigning dielectric boundaries at the interface of subunits in the filament for the implicit solvent used in electrostatic free energy evaluations. Differences in $E°$ between $C(E,pH)$MD and QM/MM@MD tended to be stochastic (of mixed sign) and similar in magnitude (<|0.160| V) to differences previously observed between $C(E,pH)$MD and experimental data on multiheme proteins.[96]

The $C(E,pH)$MD-computed $E°$'s were obtained by simultaneously sampling the redox and protonation states for all hemes in the simulated OmcS filament over a range of solution potentials at pH 7. The QM/MM@MD-computed $E°$'s, by contrast, were determined for each heme at the center of the simulated filament without permitting any other change in the redox or protonation state. When the classical simulations were repeated with either the propionic acid groups locked in the deprotonated state or the redox state of all hemes except the one being titrated fixed in the oxidized state, the zigzag pattern of $E°$'s along the heme chain was qualitatively similar (Figure S6). Thus, redox and pH cooperativities were not predicted to change the ordering of hemes by $E°$ at 300 K and pH 7.

Overall, QM/MM@MD and $C(E,pH)$MD methodologies gave a largely consistent picture of the $E°$'s in OmcS. Heme #4

was the most readily oxidized, and #1 was (or tied with #3 as) the most readily reduced heme (Tables S10 and S11). Between these extremes that spanned ~0.2 V according to both methods, #2 was more readily oxidized than #3.

The $E°$'s at 300 K in the present work and 310 K in a prior study,[80] both obtained with QM/MM@MD techniques (see Table S1 for an extensive comparison), agreed within |0.072| V for almost every heme (Table S11). This level of agreement attests to the robustness of the computed $E°$'s in both works. The exception was #5 for which $E°$ was more negative by 0.3 V in the prior study (−0.521 vs −0.214 V, both relative to SHE). The reason for this discrepancy is not entirely clear, but it likely did not result from the 10 K warmer temperature used for MD in the prior work. That supposition would require an average temperature coefficient ($\Delta E°/\Delta T$) of 0.03 V/K, which is 10 times larger than experimental values for a variety of cytochromes.[84−91]

The $E°$ for #5 in the prior study[80] was at least ~0.15 V outside the expected experimental range.[83] The value also disagreed with both $C(E,pH)$MD and the more rigorous QM/MM@MD computations by an amount at least three times larger than for any other heme. Thus, the data suggest that the $E°$ reported here for #5 is a better estimate of the true value.

The revised $E°$ for #5 significantly reduced the redox potential differences and thereby free energy changes for electron transfer to and from this heme on which Marcus theory rates exponentially depend. These Marcus rates were previously used to evaluate the charge mobility with variable time step kinetic Monte Carlo (KMC).[80] The implications of the more positive $E°$ of #5 for charge mobility are analyzed below.

3.1.2. Low (270 K) Temperature. Lowering the temperature by 30 K induced negative and nearly uniform (−0.024 to −0.101 V) shifts in $E°$ for each of the six hemes (Figure 3, orange vs blue on the *left*; Tables S3, S6, and S11). The average computed temperature coefficient of −0.002 V/K was quantitatively consistent with experimentally determined values for several other cytochromes.[84−91] Because of the uniformity of the cooling-induced shifts, there was an overall similar zigzag pattern of the $E°$'s along the heme #1 → #2 ... #6 chain at 300 and 270 K.

CEMD simulations also found negligible (|±0.032| V) shifts in $E°$ upon cooling (Table S10). This result must be treated with care, however, because it assumes, on the basis of some experiments,[97] that the $E°$ of the *N*-acetylmicroperoxidase-11 reference compound for the simulations was temperature independent. Note, too, that protonation states were held fixed (CEMD instead of ($C(E,pH)$MD)) at both temperatures in lieu of knowledge about the temperature dependencies. The CEMD result at least suggests that there was no dramatic structural transition within the protein from 300 to 270 K because the electrostatic free energies for heme oxidation were similar at both temperatures. The analysis in Section 3.2.1 below suggests that a change in the microstructure of the solvent was primarily responsible for the largest shifts in $E°$ upon cooling. This effect would be missed by CEMD because the energy evaluations were performed for the protein in a bulk aqueous dielectric.

The cooling-induced shifts in $E°$ were substantially different from the work by Dahl *et al.* (Table S11).[80] Hemes #3 and #4 in that work, for example, experienced nearly equal and oppositely signed shifts in $E°$ of −0.189 and +0.113 V even though these hemes were in van der Waals contact. This prior

study therefore reported a range of temperature coefficients that was unexpectedly large and of mixed sign (+0.004 to −0.006 V/K). The implications of the differently sized and signed shifts in $E°$ found in the present and prior works for charge mobility are analyzed below.

3.2. Microscopic Origin of Cooling-Induced Redox Potential Shifts. *3.2.1. Role of Solvent and Protein Electrostatics.* The hemes with the most to least responsive $E°$ upon cooling ($\Delta E°$) were #5 > #6 > #1 > #4 > #3 > #2. This ordering was almost perfectly reproduced (Figure 3, *right*; Table S11 and S25) by the change in electrostatic energy for oxidation of the hemes at 270 vs 300 K (ΔE_{elec}) (eq 1). The only exception was that the ordering of #1 and #4, which were in the middle of the series and had very similar shifts, was inverted for ΔE_{elec}.

$$\Delta E° \propto \Delta E_{elec}$$
$$= ((E_{elec,ox} - E_{elec,red})_{270K} - (E_{elec,ox} - E_{elec,red})_{300K})$$
$$(1)$$

where $E_{elec, ox/red}$ is the electrostatic interaction energy for a given heme in the oxidized/reduced state. ΔE_{elec} was always larger than $\Delta E°$ by a factor of 1.4 to 4.2, which likely reflected the greater sensitivity of a fixed point-charge electrostatics model to instantaneous environmental conformations.[95] All reported ΔE_{elec}'s in Figures 3 and 4 were therefore scaled by the average $\frac{\Delta E°}{\Delta E_{elec}}$ factor of 0.37 V/eV.
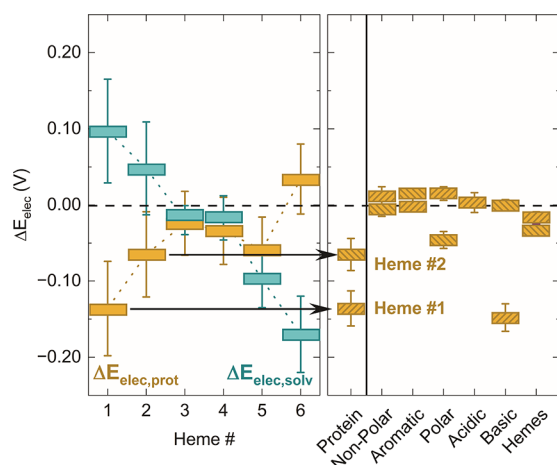
Figure 4. Decomposition of cooling-induced changes in electrostatic energy for heme oxidation into contributions from various components of the environment: (*left*) solvent and protein contributions, the sum of which gives the total shift shown in Figure 3, and (*right*) different physicochemical groupings of residues, the sum of which gives the total contribution from the protein. This latter analysis is only shown for hemes #1 and #2. Data for all hemes are given in Table S25.

Because Coulombic interactions are pairwise decomposable, ΔE_{elec} was partitioned into contributions from the solvent ($\Delta E_{elec, solv}$) and the protein ($\Delta E_{elec, prot}$). The latter contribution was further divided into influences from nonpolar, aromatic, polar, acidic, and basic residues, as well as other heme groups (Figure 4, Table S25).

Figure 4 reveals that ΔE_{elec} was negative for each heme because (1) both $\Delta E_{elec, solv}$ and $\Delta E_{elec, prot}$ were negative (hemes #3, #4, and #5), (2) $\Delta E_{elec, solv}$ was more negative than $\Delta E_{elec, prot}$ was positive (heme #6), or (3) $\Delta E_{elec, prot}$ was more

negative than $\Delta E_{elec, solv}$ was positive (hemes #1 and #2). In the latter case, altered interactions upon cooling with basic or polar residues for #1 and #2, respectively, primarily caused the negative $\Delta E_{elec, prot}$. Importantly, $\Delta E_{elec, solv}$ and $\Delta E_{elec, prot}$ were comparable in magnitude (0.03 to −0.17 eV), indicating that the solvent was an equal participant with the protein in the temperature-dependent tuning of heme redox potentials. It follows that the redox properties of the filament should be sensitive to the nature of the solvent.

This sensitivity was evidenced, for example, with respect to the microstructure of solvation shells. The negative $\Delta E_{elec, solv}$ for #5 and #6 and the positive $\Delta E_{elec, solv}$ for #2 were associated with an increased density upon cooling for solvation shells within 30 Å of the filament when these hemes were in the oxidized or reduced states, respectively (Figure 5, *top* and *middle*). Furthermore, cooling-induced shifts in $E°$ were on average smaller in magnitude by ~60% and inverted in sign for two of the hemes (#3 and #5) when an aqueous dielectric replaced the explicit solvent (Figure 5, *bottom*; Tables S3 and S6 vs S5 and S7). Thus, changes in the structure and density of solvation shells around the filament were just as important as the repositioning of protein residues for explaining the temperature dependence of $E°$'s in filamentous OmcS.

Figure 3 (*right*) directly related $\Delta E°$ computed with QM/MM@MD to ΔE_{elec} computed with classical electrostatics. Figures 4 and 5 extended this analysis to provide a microscopic explanation for the distinct temperature sensitivities of the hemes. Both the approach and insights drawn from these figures mark an advance over prior work. Previously, $\Delta E°$ was only weakly correlated ($R^2 = 0.51-0.65$) with changes in the planarity of the heme macrocycles or the electric field exerted on the Fe centers.[80] Both effects were attributed to a cooling-induced restructuring of the intraprotein H-bonding network, a phenomenon examined in the next subsection.

3.2.2. Role of Intraprotein H-Bond Restructuring. Previously, $\Delta E°$ was rationalized in terms of intraprotein H-bond restructuring. The restructuring was quantified in terms of the norm of a H-bonding occupancy matrix (dubbed the characteristic H-bonding frequency, CHF) at a given temperature and the norm of a difference matrix (dubbed ΔCHF) between two temperatures. These metrics are shown in Figure 6 (*top*) over a wider temperature range (100−400 vs 270−310 K) than originally reported.[80] The ΔCHF was computed at each temperature relative to 300 K, where it therefore had a value of zero (no difference). In addition, the norm of the difference matrix filtered to contain only the occupancies of H-bonds common to 300 K and some other temperature (ΔCHF$_{shared}$) is shown in the figure.

Between 300 and 270 K, where filamentous OmcS exhibits *anti*-Arrhenius conductivity, the CHF and ΔCHF changed respectively by 0.8 and 4.4 in the present study. Similar changes of 1.0 and 6.2 were found in the prior work between 310 and 270 K.[80]

In general, a linear dependence ($R^2 = 0.9969$) of the CHF on temperature over the 100−400 K range was found (Figure 6, *top*; Table S26): CHF = 19.1(± 0.1) − 0.0273(± 0.0004)T. This result paralleled a linear dependence ($R^2 = 0.9778$) of the number of H-bonds on temperature according to the equation (Figure 6, *bottom*; Table S24): # of H-bonds = 420(± 6) − 0.50 (± 0.02)T. Thus, temperature was more like a "dial" than a "switch"[80] for the overall occupancy of the H-bonding network. However, a straightforward connection between the monotonic (Figure 6, *bottom*) and bell-shaped
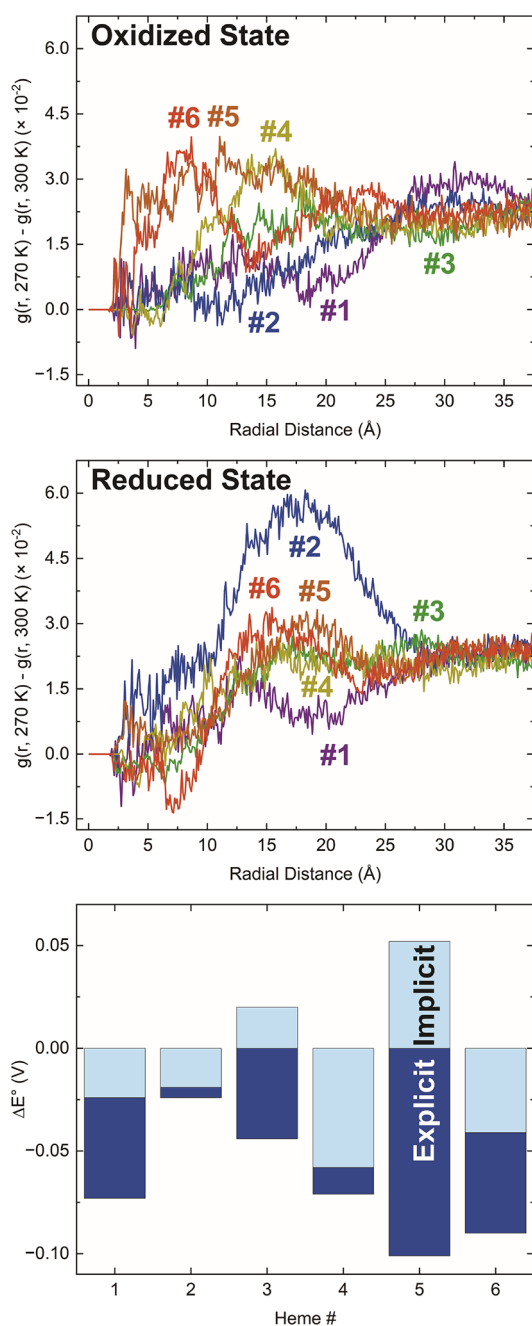
Figure 5. Cooling-induced effects on heme redox potentials depend on the microscopic solvent structure. Change in radial distribution functions ($g(r, T)$) for the solvent with respect to each heme in the (*top*) oxidized and (*middle*) reduced redox states. $g(r, T)$ was normalized to the density of pure water (0.033456 molecules/Å^3). (*Bottom*) Cooling-induced redox potential shifts in the presence of an explicit or implicit (bulk aqueous dielectric) solvent. At both temperatures, each heme, the other hemes and protein, and solvent were respectively modeled with B3LYP/[Fe = LANL2DZ; H, C, N, S = 6-31G(d)], AMBER99SB, and either TIP3P (explicit solvent) or Poisson−Boltzmann surface area (PBSA) reaction field charges (implicit solvent).

Figure 6. Variation in intraprotein H-bonding with temperature. (*Top*) Variation with temperature in the characteristic H-bonding frequency (CHF), the difference (ΔCHF), and the ΔCHF only considering H-bonds present at 300 K and some other temperature (ΔCHF$_{shared}$). (*Bottom*) Change in the number and occupancy of intraprotein H-bonds as a function of temperature.

(Figure 1, *bottom*) dependencies of H-bonding and electrical connectivity on temperature was not obvious.

The larger magnitude of ΔCHF compared to the change in CHFs between two temperatures (i.e., the norm of a difference matrix vs the difference in norms of individual matrices) was

interpreted in the prior work as a "massive restructuring" of the H-bonding network.[80] However, the term "restructuring" is potentially misleading. Both the prior and present studies found <10% of H-bonds to be unique to either high (300 or 310 K) or low (270 K) temperature simulations.

In the simulations reported here, 66% of H-bonds had <10% change in occupancy (including from zero), and another 20% of H-bonds were common to both temperatures but experienced larger changes in occupancy (Figure 6, *bottom*; Table S24). Thus, the data suggest that the connectivity of the H-bonding network was largely preserved, not restructured, between 300 and 270 K.

Only 9 and 5% of the remaining H-bonds were unique to 270 or 300 K, respectively, and had an occupancy >10%. Of these unique H-bonds, fewer than a dozen occurred within 10 Å of the hemes at the center of the filament (Tables S27−S29) for which $E°$'s were computed. Given this observation, it seems unlikely that restructuring in H-bonds, taken alone, can account for significant shifts in the $E°$'s of the hemes upon cooling.

With virtually identical metrics for the change in H-bonding upon cooling as found in the present work, the prior study[80] reported a maximal change in $E°$ that was twice as large as found here (∼0.2 V) and one-fourth the entire biological range of heme redox potentials.[83] This comparison suggests that

changes in intraprotein H-bonding were not the controlling factor for the temperature sensitivity of the $E°$'s. The controlling factors were diagnosed in the previous section as the microstructure of the solvent and the arrangement of protein residues that exert different electrostatic influences on the hemes upon cooling.

These findings further suggest that an interpretation different from H-bond restructuring may apply to a previously reported kinetic isotope effect (KIE).[80] A 3- to 300-fold reduction in conductivity was reported upon deuteration of films of OmcS filaments. KIEs ≥130 for OmcS in the 230−260 K range were reminiscent of those ascribed to concerted electron−proton transfer in wild-type soybean lipoxygenase (KIE = 81)[98] and proton coupled electron transfer (PCET) in a benzoquinone and Os(IV)-hydrazido complex (KIE = 455).[99] In the context of PCET, large KIEs reflect the fact that the two-times greater mass of the deuteron vs proton causes more localized vibrational wavefunctions, decreased wavefunction overlaps, and thereby reduced tunneling probabilities.[100]

On a classical electrostatics level, CpHMD simulations in the present work indicated that changes in pK_a's were coupled to the redox processes (Table S13) so as to compensate for the change in charge.[101] The net charge of the protein changed by only ∼50% of the expected amount in the physiologically relevant 5 to 7 pH range upon reduction of the six central hemes in the filament (Table S14; Figure S7). This charge-compensation effect was determined by computing the pK_a's for all 82 titratable residues within the central subunit of the filament before and after a six-electron reduction of the hemes in that subunit (Table S13) and applying the Henderson−Hasselbalch equation at different pHs.

It is possible that the coupling of electron and proton transport—an aspect neglected in all conductivity modeling to date for OmcS—may help to bridge the discrepancy between the observed and simulated currents (see below discussion). Indeed, transport of both electrons and protons was invoked to rationalize[40] the increased electrical conductivity observed for pili[37]/OmcS[56] filaments as the pH was lowered.

3.3. Temperature Dependence of Heme-to-Heme Reaction Free Energies. Using the computed $E°$'s just discussed, Figure 7 compares the resulting free energy (ΔG_{mn}; m = donor, n = acceptor) landscapes for heme-to-heme electron transfer at high (300 or 310 K) and low (270 K) temperatures with prior work.[79,80]

ΔG_{mn}'s found in the present study were −0.097 to +0.190 eV at 270 or 300 K and differed by at most |0.05| eV at the two temperatures (Table S19). The range was considerably smaller than the −0.441 to +0.256 eV reported in the work by Dahl et al.[80] at 270 or 310 K but in very close agreement with the work of Jiang et al.[79] at 300 K (−0.090 to +0.120 eV). The larger range found by Dahl et al. primarily resulted from an $E°$ that was too far negative by 0.3 V at 310 K,[80] as discussed above. Dahl et al.[80] also predicted a six-times larger (∼|0.3| eV) change in ΔG_{mn} between 310 and 270 K because the $E°$'s for two adjacent hemes were predicted to shift in opposite directions by >|0.1| V.

The individual ΔG_{mn}'s at 300 K in the current study generally differed by ≤0.1 eV with respect to all prior work at high temperature (Figure 7, left), which was quite reasonable given the different methodologies that have been used.[79,80] The only exception with respect to the work of Jiang et al.[79] was for $\Delta G_{6,1}$ (|0.1| eV). In that work, there may have been
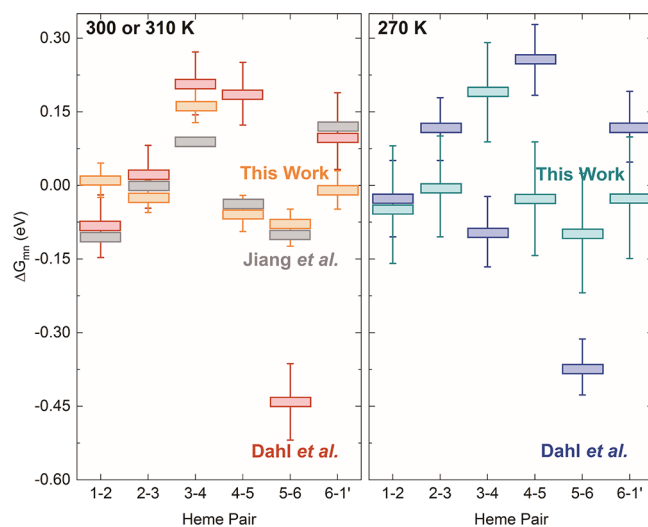
Figure 7. Temperature dependence of free energy landscapes for heme-to-heme electron transfer. (Left) High (300 or 310 K) and (right) low (270 K) temperatures. At high temperature, the results of the present study and those by Jiang et al. pertain to 300 K; the work by Dahl et al. was conducted at 310 K.

difficulties in assigning dielectric boundaries for the implicit solvent at the interface of subunits where #6 and #1 reside. A similar issue was already noted when comparing $E°$'s from C(E,pH)MD and QM/MM@MD. Larger deviations were found at high temperature with respect to the work of Dahl et al.[80] for $\Delta G_{4,5}$ (|0.25| eV) and $\Delta G_{5,6}$ (|0.35| eV), likely because of the too-far negative $E°$ for #5.

At 270 K (Figure 7, right), the ΔG_{mn}'s in the present study deviated from the report of Dahl et al.[80] by ∼|0.13| eV for $\Delta G_{2,3}$ and $\Delta G_{6,1}$ and by ∼|0.28| eV for $\Delta G_{3,4}$, $\Delta G_{4,5}$, and $\Delta G_{5,6}$. The origin of these large differences is not clear but may reflect, in part, insufficient sampling in the earlier work. For reference, the mean unsigned error for the ΔG_{mn}'s in the present study was half as large as for Dahl et al., both at high temperature, relative to the work of Jiang et al.[79]

3.4. Temperature Dependence of Redox Conductivity. Filamentous OmcS resembles other redox chains in biology—albeit on a much longer length scale (μm instead of nm)—in that the filament connects discrete electron donors (unidentified) and acceptors (e.g., Fe(III) or Mn(IV) oxide nanoparticles). In between the primary donor and ultimate acceptor, electrons are thought to nonadiabatically tunnel from heme-to-heme in a multistep process under physiological (not necessarily solid-state) conditions.[70−73,102]

This "hopping" regime of electron transfer is well-described by the Marcus theory.[76,77] As shown in eq 2, the Marcus rate for each electron transfer step (k_{nm}) depends on the free energy change for the reaction (ΔG_{mn}), the reorganization energy for the polarization response of the nuclei (λ_{mn}), and the electronic coupling between the electron donor and acceptor (H_{mn}). Note that the convention is to specify the donor and acceptor from right to left for the rate constant but left to right for the energetic terms. k_b, T, $\hbar$, and $\langle...\rangle$ in eq 2 signify, respectively, the Boltzmann constant, absolute temperature (taken to be 300 or 270 K), reduced Plank constant, and thermal averaging. As already discussed, ΔG_{mn} in eq 2 was determined from the difference in $E°$ between adjacent hemes.

A particular focus was given above on describing high-quality estimates of $E°$ at 300 and 270 K because each k_{nm}

exponentially depends on ΔG_{mn}. Unlike ΔG_{mn} (Table S19), λ_{mn} and H_{mn} were much less sensitive to a change in temperature and agreed within the same order of magnitude with prior work (Tables S20 and S22), as discussed more in Sections S2 and S3 of the SI.

$$k_{nm} = \frac{2\pi\langle H_{mn}^2\rangle e^{-(\Delta G_{mn}^{\circ}+\lambda_{mn})^2/4\lambda_{mn}k_b T}}{\hbar\sqrt{(4\pi\lambda_{mn}k_b T)}} \qquad (2)$$

Using the estimates of ΔG_{mn} discussed in the previous section, along with computed values for λ_{mn} and $\langle H_{mn}\rangle$, Marcus rates were evaluated in the forward (#1 → #2 ... → #6) and reverse (#6 → #5 ... → #1) directions (Table S23) and compared to prior work (Section S4 in the SI). These rates were assembled into kinetic models to simulate the electron current (Tables S31 and S32). Similar modeling efforts have already been described for OmcS.[79−81] To aid comparison with these studies, both single-particle diffusion[80,81] and multiparticle steady-state flux[103] models were used in the present study.

In the outlined approach, there are multiple levels of temperature dependences: ΔG_{mn}, λ_{mn}, and H_{mn} were evaluated from MD simulations at 300 or 270 K. The k_{nm}'s evaluated with these quantities explicitly have a $T^{-1/2}e^{T^{-1}}$ dependence (eq 2). For the computation of an electrical current from single-particle diffusive kinetics, the current has a further T^{-1} dependence (eq S10).

3.4.1. Single-Particle Diffusive Kinetics.
Figure 8 compares the AFM-measured current[80] and the theoretical diffusive
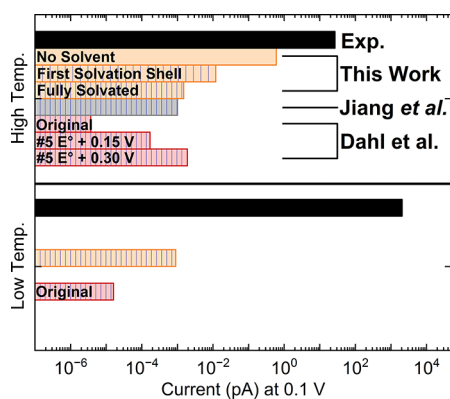
Figure 8. Comparison of experimental currents (ref 80) with simulated diffusive hopping currents computed from Marcus theory rates provided in the present and prior studies (refs 79 and 80). Absent, sparse, or dense vertical stripes indicate the level of solvation. "Original" means that the energetic parameters were used as reported in ref 80. "#5 E° +..." indicates a shift applied to the reported redox potential of heme #5 while keeping all other energetic parameters at the reported values.

hopping current for an applied bias of 0.1 V at high (300 or 310 K) and low (270 K) temperature, as well as for different extents of solvation. Because the 0.1 V drop was applied experimentally over a filament at least 300 nm long, the imposed bias between adjacent hemes was much less than the thermal energy. The employed diffusion model is valid in this zero-field limit. The diffusion model also assumed single or noninteracting mobile charges, a restriction relaxed in the multiparticle flux approach used below.

An immediate observation from Figure 8 is that the theoretical hopping currents—regardless of which set of Marcus rates is used—severely underestimate the experimental current. All models that include the reorganization energy contributed by the aqueous solvent in the fully hydrated state predicted currents that were 4 to 6 orders of magnitude too small (Table S32).

This discrepancy was already foreseen by Amdursky and co-workers.[81] These authors proposed that either the reorganization energy accompanying electron transfer was unusually low for biological systems (∼0.15 eV) or the rigidification of the protein scaffold preserved coherences among blocks of heme groups to assist the incoherent charge hopping process.

Because loops and turns comprise 81% of the secondary structure of OmcS[104] and the interheme electronic coupling is less than the thermal energy at 298 K (Table S22), it is difficult to envision how coherence over a 20 nm stretch of hemes, as proposed,[81] can be maintained.

The other (unusually low reorganization energy) hypothesis may be realized in the partially dehydrated state of OmcS under experimental conditions. In this view, the incoherent hopping mechanism may appear insufficient because simulations of an OmcS oligomer in salt solutions—what all studies have used to date—are of little relevance for modeling charge transport through an electrode-adsorbed, (partially or fully) dehydrated, and (possibly) aggregated protein.

Ru[105] noted that dehydration of the protein "nanowire" likely removes a significant fraction,[106] perhaps as much as 50%,[107] of the outer-sphere reorganization energy. Indeed, the activation energies for electron transfer in solution-phase simulations of filamentous OmcS were dominated by λ_{mn}, a large fraction of which came from the aqueous solvent (Table S21 and S30).

When none of the reorganization energy contributed from the aqueous solvent or only the portion due to the first solvation shell (∼3400 waters and 12 Na$^+$ ions within 3.4 Å of the filament) was included, the predicted current was a few orders of magnitude closer to experiments (Figure 8). The amount of solvent present in the conductivity experiments for OmcS has not been rigorously controlled or characterized. AFM experiments were performed on filaments that appeared "dry", but the computations indicate that the amount of reorganization energy is highly sensitive to the number of water molecules within 1.0 nm of the filament (Table S30; Figure S9), which was below the spatial resolution of the employed instrument.

Other important observations from Figure 8 are as follows: (1) Simulated hopping currents at 300 K in the present study agreed (within a factor of 2) with the work by Jiang et al.[79] (2) The current at 310 K for the work by Dahl et al.[80] was 2 orders of magnitude smaller than the results presented here. (3) The discrepancy was largely removed by shifting the previously reported E° for #5 by +0.15 V. This shift was how much the previously reported E° exceeded the most negative potential expected for a bis-histidine-ligated c-type heme (−0.350 V vs SHE). A further shift of +0.15 V would be needed to match the E° computed in the present work (Table S11) and would cause an even greater increase in the predicted current at 310 K (Figure 8). (4) From 310 to 270 K, the current for Dahl et al.[80] increased by a factor of 4. The increase was smaller than the reported factor of 72 likely because the previous work mistakenly averaged mean-squared displacements from variable time step KMC simulations over the *number* of unequally

sized time increments (number of MC steps).[80,108,109] The present study used instead an analytical formula derived by Derrida and implemented by Jansson[110,111] (see Section S1.6.1 in the SI) to obtain the diffusion constant for the same physical system: a one-dimensional periodic chain of hopping sites. The analytical and KMC methods should agree in the limit of converged statistics for the latter approach. (5) The current instead decreased by a factor of 11 for Dahl *et al.* if the $E°$ for #5 at 310 K was shifted by +0.15 V while keeping all other energetic parameters the same. (6) The current computed in the present study similarly decreased by a factor of 2 from 300 to 270 K.

Thus, Figure 8 indicates that a hopping model premised on diffusive particle kinetics, governed by standard Marcus theory rates (eq 2), fails to capture the *anti*-Arrhenius temperature dependence of electrical conductivity in filamentous OmcS. The previous reproduction of *anti*-Arrhenius behavior seems to have resulted, in part, from an underestimation of the conductivity at high temperature because of a too-far negative $E°$ for #5, which in turn caused the conductivity at low temperature to appear larger by comparison.

The failure to describe even qualitatively the *anti*-Arrhenius behavior, like the comparison of absolute conductivities, may reflect the influence of solvation. Variations in experimental conditions including hydration have been implicated in the observation of different temperature dependences.[112−114] The bell-shaped pattern reported by Dahl *et al.*[80] (Figure 1, *bottom*) was observed earlier—albeit ascribed to pili at the time—under similar conditions.[37] At temperatures above 270 K, however, a much weaker increase[115] or even a decrease[116] in conductivity upon cooling was reported under different conditions. The moisture/water content was shown in the context of *G. sulfurreducens* biofilms to determine whether an increase or decrease in conductivity was observed with decreasing temperature.[113] In kinetic isotope experiments at different temperatures,[80] a sharp change in conductance at 220 K for only the deuterated sample was ascribed to the dynamical protein transition, which is intimately related to the hydration shell of the protein.[117]

3.4.2. Multiparticle Flux Kinetics. Essentially all of the foregoing conclusions from the single-particle diffusion model were reproduced with the flux kinetic scheme (Tables S31 and S32). Additionally, the flux model provided an estimate of the protein-limited current and the voltage needed to attain it.

The protein-limited current (Figure S8) was realized at an injection/ejection rate (assumed to be symmetric) of 10^{10} electrons/s or, equivalently, 1.6×10^{-9} A. The associated voltage for passing this current through the filament can be obtained by considering the experimentally reported resistance. The filament was reported to have a resistance of 2.3×10^8 Ω/subunit and a contact resistance (both termini) of 1.2×10^9 Ω.[80] For the simulated OmcS trimer, the total resistance would be (3 subunits × 2.3×10^8 Ω/subunit) + 1.2×10^9 Ω = 1.9×10^9 Ω. The voltage needed to realize protein-limited current was therefore given by Ohm's law as ((1.6×10^{-9} A) × (1.9×10^9 Ω)) = 3.0 V.

The predicted protein-limited current at this voltage was <1 pA, whereas the experimentally measured current at a voltage 30 times smaller was reported to be ∼27 pA.[80] The enormous discrepancy was also found regardless of whether the Marcus rates reported by Jiang *et al.* or Dahl *et al.* were used to evaluate the flux kinetic model.

3.4.3. Conclusion from Single- and Multiparticle Kinetics. A charge hopping model fails to quantitatively, or qualitatively as a function of temperature, describe electrical conductivity in filamentous OmcS. This conclusion is seemingly at odds with the reported linear dependence of conductance on filament length,[80] but this is not an unambiguous metric for deciding the charge transport mechansim.[118] Still, a verdict in favor of coherence-assisted hopping[81] or decoherent quantum transport[82] over incoherent charge hopping[79,80] should await simulations that more nearly capture the physical conditions—especially the extent of solvation—present in experiments.

3.5. Mechanistic Precedents for *Anti*-Arrhenius Electron Transfer. An *anti*-Arrhenius temperature dependence, as found for electrical conductivity in filamentous OmcS between 270 and 300 K (Figure 1, *bottom*), reflects a negative apparent activation enthalpy ($\Delta H^{\ddagger}$). Marcus demonstrated (eq 3) that a negative $\Delta H^{\ddagger}$ results if the enthalpic change for a reaction ($\Delta H°$) is sufficiently negative and/or if the entropic change for the reaction ($\Delta S°$) is sufficiently large (positive or negative).[119,120]

$$\Delta H^{\ddagger} = \frac{(\lambda + \Delta H°)^2}{4\lambda} - \frac{(T\Delta S°)^2}{4\lambda} \tag{3}$$

Equation 3 is a consequence of the fact that parabolic enthalpy curves for the reactant and product states are displaced from the corresponding free energy curves when $\Delta S° \neq 0$. The equation was derived assuming equal-curvature parabolas, weak donor−acceptor electronic couplings, and temperature-independent reorganization energies—all of which reasonably apply to filamentous OmcS based on the presented computations (Figures S1 and S3; Tables S20 and S22).

There are a plethora of ways entropic effects may contribute to the observed *anti*-Arrhenius—and, more generally, bell-shaped—temperature dependence of electrical conductivity. Virtually all the examples surveyed in the following subsections involve simpler systems (e.g., a single-step electron transfer or a single energy level in theoretical work), so a quantitative explanation for the behavior in OmcS cannot be expected. The hope, however, is that this unique summary of interpretations for *anti*-Arrhenius phenomena will inspire new experiments on OmcS.

3.5.1. Change in Quantum State Spacing. Marcus and Sutin used eq 3 to explain[119,120] the *anti*-Arrhenius temperature dependence of electron transfer between $Fe(H_2O)_6^{2+}$ and Fe^{3+} or Ru^{3+} polypyridine complexes.[121,122] The measured negative $\Delta H°$ and $\Delta S°$ indicated that the product quantum states were shifted to a lower energy and were more widely spaced than those of the reactants (see Figure 1 in ref 120). If these shifts were large enough, the Boltzmann-averaged enthalpy of the activated complex could fall below the Boltzmann-averaged enthalpy of the reactant state. In this scenario, the lower-energy reactant quantum states would react more readily than the higher-energy ones, giving an *anti*-Arrhenius temperature dependence. Temperature-dependent experiments to dissect the enthalpic and entropic contributions to electron transfers in OmcS are needed to probe the applicability of this explanation.

3.5.2. Change in Vibrations Coupled to Electron Transfer. A change in the vibrational density of states was invoked to explain the *anti*-Arrhenius behavior of electron transfer in

bacterial photosynthetic reaction centers.[123,124] An increase in rate upon cooling for these activationless reactions was explained in terms of a transfer of population from higher to lower vibrational energy levels in the reactant and product states. The lower energy vibrations had larger Frank–Condon overlap factors, and Marcus theory rates were directly proportional to the Frank–Condon weighted density of states. Changes in frequency for hydrational, porphyrin skeletal, or protein vibrations coupled to the electron transfer were also needed to account for the experimental data.

Similarly, high-frequency intramolecular vibrations that need to be treated quantum mechanically were found to couple to electron transfer in an organic semiconductor and to result in an *anti*-Arrhenius temperature dependence.[125]

In the context of cytochrome *c* adsorbed to a self-assembled monolayer (SAM)-coated electrode, Matyushov pointed out that thermally induced oscillations of the protein-electrode distance introduce temperature-dependent contributions to the activation enthalpy and entropy.[126] At high enough temperatures, the entropic term in an equation analogous to eq 3 (eq 65 in ref 126, which originates from the mean-squared displacement of the protein atoms, is anticipated to cause a negative activation energy, or *anti*-Arrhenius behavior.

Thus, the modeling of filamentous OmcS may fail to capture the *anti*-Arrhenius phenomenon because the classical (high-temperature limit) for thermally populated vibrations assumed in eq 2 may not be valid at 300 and 270 K. The vibrations sampled by filamentous OmcS at these temperatures in solutions vs adsorbed on an electrode in a partially dehydrated state may also be different.

3.5.3. Stereodynamical and Roaming Effects. Anti-Arrhenius kinetics were observed in the reaction of hydroxyl radical with HBr because increased thermal agitation disfavors the narrow range of reactive geometries and promotes "roaming" among vibrational modes.[127,128] Configurations of filamentous OmcS that promote electron transfer may be attained at lower temperatures. However, the modeling suggests that sufficiently large structural transitions, if they occur, require a time scale that exceeds $\sim 10^2$ ns and therefore have not been observed in theoretical studies to date.

3.5.4. Change in Medium Relaxation Modes. Dipolar orientations and translations are two important collective modes of a polar medium that respectively make enthalpic and entropic contributions to the donor–acceptor energy gap.[129] Dipolar translations manifest as density fluctuations. The foregoing analysis (Figure 5) indicated that the density of the solvation shells changes upon cooling in a redox-state dependent fashion.

Matyushov and co-workers[129,130] showed that dipolar orientations and translations of the solvent impart hyperbolic temperature dependencies, with opposite signs, to the reaction and reorganization free energies. These dependences are manifested when the solvent response is not quasi-macroscopic,[131] which may describe the case of a partially dried protein sample as in the temperature-dependent experiments. The result is a transition from *anti*-Arrhenius to Arrhenius kinetics upon cooling. This effect was used to explain the bell-shaped temperature dependence of charge recombination in a porphyrin-bridge-fullerene complex.[129]

Cooling can also slow or even arrest relaxation modes of the medium that are coupled to electron transfer. Nitzan and co-workers[132] found that the average current for hopping conduction under low applied bias (0.1 V) can switch from

a direct to inverse proportionality on the solvent relaxation time (γ) as γ increases. Given that γ, or the viscosity of the medium, increases with decreasing temperature, this finding predicts a switch from an *anti*-Arrhenius to an Arrhenius dependence of the current as the temperature is lowered.[133]

Nitzan and co-workers dubbed this phenomenon a "Kramers'-like turnover" in recognition of Kramers' rate theory,[134] which describes solvent-controlled dynamics when the relaxation time of the medium is comparable to the passage time through the transition state region along the reaction coordinate. Kramers' turnovers have been used to explain the *anti*-Arrhenius-to-Arrhenius temperature dependence of *trans*-to-*cis* photoisomerization of stilbene and the positronium quenching rate constant for formation of a positronium–acceptor complex[133] and may be relevant to OmcS. However, a problem with this hypothesis is that the exponential in eq 2 is usually more sensitive to changes in temperature than the pre-exponential, which acquires the dependence on γ.

If the temperature is lowered enough, some of the medium relaxation modes can become dynamically arrested. Below a crossover temperature, the dynamics of the protein are non-ergodic, and the reorganization energy decreases (instead of increasing as expected) upon further cooling.[135] Tables S21 and S30 in the SI indicate that ergodicity is broken for filamentous OmcS even at 300 K in a partially or fully dehydrated condition, a result consistent with work on electrode-adsorbed azurin.[136] Ergodicity breaking was able to explain the *anti*-Arrhenius temperature dependence of self-exchange electron transfer in mixed-valence complexes as the temperatures neared the point of solvent crystallization.[135]

Thus, extensions to standard Marcus theory that consider the microscopic nature of solvation and the change in time scales for medium relaxation modes upon cooling may be needed to model the *anti*-Arrhenius conductivity observed for OmcS.

3.5.5. Redox State-Dependent Solvation. Another way the solvent can produce a bell-shaped Arrhenius plot is if the solvent differentially wets one of the two charge states of the redox protein. In the case of ferredoxin, the temperature dependence of the reorganization energy, attributed to preferential wetting of the reduced state, produced a bell-shaped dependence of the activation energy on inverse temperature.[137]

In Figure 5 for OmcS, the density of the solvation shells increased for #5 and #6 in the oxidized state and #2 in the reduced state. Application of the theory in ref 137 to these redox-state dependent differences in solvation for filamentous OmcS may help to explain the *anti*-Arrhenius conductivity.

3.5.6. Energy Level Renormalization in a Molecular Junction. Marcus showed that the inclusion of entropic effects results in a temperature-dependent shift in the position of the molecular energy level relative to the electronic states of the electrodes.[138] The result is an *anti*-Arrhenius temperature dependence in the off-resonant and resonant regimes for electron transport through a molecular junction device.

3.5.7. Thermally Assisted Tunneling. A highly speculative proposal is that the *anti*-Arrhenius-to-Arrhenius temperature dependence of conductivity in OmcS reflects a crossover from thermally activated to tunneling transport upon cooling.[139]

Thermally activated over-barrier crossings dominate at high temperature, whereas through-barrier tunneling dominates at low temperature. The crossover temperature (T_c) from over- to through-barrier mechanisms depends on the specific

reaction; for hydrogen atom transfers, T_c is commonly near room temperature.[140]

The overall reaction rate in the intermediate range between the high- and low-temperature extremes often exceeds the (extrapolated) thermal rate and the low-temperature tunneling limit combined, a phenomenon dubbed temperature-assisted tunneling or vibrationally activated tunneling.[140,141] A consequence of this effect is typically a convex instead of a linear line in an Arrhenius $\ln(k_{nm})$ vs $1/T$ plot, which is called "sub-Arrhenius" behavior.[142] If the increase in through-barrier tunneling with cooling can overcompensate for the decrease in over-barrier transitions, perhaps an *anti*-Arrhenius temperature dependence can be observed down to T_c. Below T_c, the conductivity may appear to decrease as in Figure 1 (*bottom*) because one of the transport channels (over-barrier transitions) has now been completely shut down.

An analogous explanation was advanced for the *anti*-Arrhenius-to-Arrhenius temperature dependence of heterogeneous ammonia synthesis in the presence of an electric field.[143] Associative and dissociative mechanisms were proposed to be operative below 373 K and above 573 K, respectively, and both exhibit Arrhenius-type dependencies on temperature. Between 373 and 573 K, both mechanisms were proposed to be operative to some extent to explain the *anti*-Arrhenius temperature dependence.

4. CONCLUSIONS

The present study characterized theoretically the temperature sensitivity of the energetics for electron transfer in filamentous OmcS. A 30 K drop in temperature was found to be a weak perturbation, changing the electronic coupling ($\langle H_{mn} \rangle$), reaction free energy (ΔG_{mn}), reorganization energy (λ_{mn}), and activation energy (E_a) by at most |0.002|, |0.050|, |0.120|, and |0.045| eV, respectively. The temperature dependence of ΔG_{mn} reflected negative and nearly uniform shifts in redox potentials ($\Delta E^{\circ\prime}$'s) that were well explained by cooling-induced changes in electrostatic energy for heme oxidation, which in turn originated from the aqueous solvent and protein in almost equal proportions. Strikingly, $\Delta E^{\circ\prime}$'s were 60% smaller in magnitude by substituting a bulk aqueous dielectric for the explicit solvent.

Biologically relevant and theoretically modeled redox conduction underestimated the AFM-measured current by 4−6 orders of magnitude at 300 K and predicted a 2-times smaller, instead of a 75-times larger, current at 270 K as reported in prior experiments and computations.[80] The inadequacy of redox conduction to explain the AFM measurements has been observed before, and taken together, the results suggest that some non-biologically relevant charge transport mechanism is operative under the experimental conditions. Underscoring this conclusion, $\sim 10^1$ pA currents at 0.1 V bias measured for a single filament by AFM are 10^2 times larger than the $\sim 10^1$ fA currents generated by an entire *G. sulfurreducens* cell.[35]

Unfortunately, the prior modeling of *anti*-Arrhenius behavior now seems to have been an artifact of (1) a severe underestimation of the conductivity at high temperature because of an unphysically negative E°, which in turn caused the conductivity at low temperature to appear larger by comparison, and (2) a mistaken implementation of variable time step KMC whereby mean-squared displacements were averaged over the *number* of unequally sized time increments (number of MC steps). Also, cooling-induced changes in H-

bonding observed in the present work virtually reproduced the earlier observations[80] even though differently sized and signed $\Delta E^{\circ\prime}$'s were observed. These changes—largely in terms of H-bonding occupancy and not connectivity as claimed before—do not, therefore, uniquely control the heme redox potentials and cannot explain *anti*-Arrhenius conductivity.

The failure of all incoherent hopping models to date may reflect the inadequacy of either[81,105] the charge transport mechanism or the modeling of dried and electrode-absorbed filaments in experiments by solution-phase simulations. Simulated hopping currents increased by a few orders of magnitude by neglecting most or all of the reorganization energy contributed by the solvent, and non-ergodicity effects—a possible mechanism for *anti*-Arrhenius kinetics—became important in partially dehydrated states. Better (experimental and theoretical) characterization of how conductivity depends on physical conditions is suggested to be essential before a verdict can be reached on the operative charge transport mechanism.[114]

In addition to refining the physical model, extensions to "vanilla" Marcus theory (eq 2)[144] are suggested to be important for the reproduction of the *anti*-Arrhenius behavior. Aspects to be considered in future work include cooling-induced effects on proton−electron coupling, changes in the vibrational density of states and the microstructure of the aqueous solvent, redox-linked differential wetting of the filament, a transition from under- to overdamped or dynamically arrested medium relaxation modes, and renormalization of molecular energy levels in an electrical device.

■ ASSOCIATED CONTENT

ⓢ Supporting Information

The Supporting Information is available free of charge at https://pubs.acs.org/doi/10.1021/acs.jpcb.2c06822.

> Theoretical background and computational details, calculation of redox potentials, electron transfer parameters, charge diffusion and fluxes, H-bond composition, and pK_a's (PDF)

■ AUTHOR INFORMATION

Corresponding Author

Matthew J. Guberman-Pfeffer − *Department of Molecular Biophysics and Biochemistry, Yale University, New Haven, Connecticut 06510, United States; Microbial Sciences Institute, Yale University, West Haven, Connecticut 06516, United States;* ⓞ orcid.org/0000-0002-1143-0693; Email: matthew.guberman-pfeffer@yale.edu

Complete contact information is available at:
https://pubs.acs.org/10.1021/acs.jpcb.2c06822

Author Contributions

The research described herein was initiated and conducted solely by the corresponding author. Acknowledgments are given below to others who provided insightful advice on related questions.

Notes

The author declares no competing financial interest.

■ ACKNOWLEDGMENTS

ABBREVIATIONS

AFM, atomic force microscopy; CE, constant redox; CHF, characteristic H-bonding frequency; CpH, constant pH; KIE, kinetic isotope effect; KMC, kinetic Monte Carlo; MD, molecular dynamics; OmcS, outer-membrane cytochrome type S; PBSA, Poisson–Boltzmann surface area; PCET, proton coupled electron transfer; QM/MM@MD, quantum mechanics/molecular mechanics at molecular dynamics-generated configurations; redox, reduction–oxidation; SAM, self-assembled monolayer; SHE, standard hydrogen electrode; VAT, vibrationally assisted tunneling

REFERENCES

(1) Torres, C. I.; Marcus, A. K.; Lee, H. S.; Parameswaran, P.; Krajmalnik-Brown, R.; Rittmann, B. E. A Kinetic Perspective on Extracellular Electron Transfer by Anode-Respiring Bacteria. *FEMS Microbiol. Rev.* **2010**, *34*, 3–17.

(2) Matyushov, D. V. Protein Electron Transfer: Is Biology (Thermo) Dynamic? *J. Phys. Condens. Matter* **2015**, *27*, No. 473001.

(3) Nealson, K. H.; Conrad, P. G. Life: Past, Present and Future. *Philos. Trans. R. Soc. London, Ser. B* **1999**, *354*, 1923–1939.

(4) Vargas, M.; Kashefi, K.; Blunt-Harris, E. L.; Lovley, D. R. Microbiological Evidence for Fe(III) Reduction on Early Earth. *Nature* **1998**, *395*, 65–67.

(5) Ilbert, M.; Bonnefoy, V. Insight into the Evolution of the Iron Oxidation Pathways. *Biochim. Biophys. Acta* **2013**, *1827*, 161–175.

(6) Zhao, J.; Li, F.; Cao, Y.; Zhang, X.; Chen, T.; Song, H.; Wang, Z. Microbial Extracellular Electron Transfer and Strategies for Engineering Electroactive Microorganisms. *Biotechnol. Adv.* **2021**, *53*, No. 107682.

(7) Lovley, D. R.; Holmes, D. E. Electromicrobiology: The Ecophysiology of Phylogenetically Diverse Electroactive Microorganisms. *Nat. Rev. Microbiol.* **2022**, *20*, 5–19.

(8) Nealson, K. H.; Saffarini, D. Iron and Manganese in Anaerobic Respiration: Environmental Significance, Physiology, and Regulation. *Annu. Rev. Microbiol.* **1994**, *48*, 311–343.

(9) Jelen, B. I.; Giovannelli, D.; Falkowski, P. G. The Role of Microbial Electron Transfer in the Coevolution of the Biosphere and Geosphere. *Annu. Rev. Microbiol.* **2016**, *70*, 45–62.

(10) Jiang, Y.; Shi, M.; Shi, L. Molecular Underpinnings for Microbial Extracellular Electron Transfer during Biogeochemical Cycling of Earth Elements. *Sci. China Life Sci.* **2019**, *62*, 1275–1286.

(11) Zhang, X.; Yuan, Z.; Hu, S. Anaerobic Oxidation of Methane Mediated by Microbial Extracellular Respiration. *Environ. Microbiol. Rep.* **2021**, *13*, 790–804.

(12) Reyes, C.; Meister, P. The Role of Microorganisms in Iron Reduction in Marine Sediments. In *Systems Biogeoichestry of Major Marine*; Mazumdar, A.; Ghosh, W., Eds.; John Wiley & Sons, Inc.: New Jersey, 2022; pp 41–60, DOI: 10.1002/9781119554356.ch3

(13) Lovley, D. R. Syntrophy Goes Electric: Direct Interspecies Electron Transfer. *Annu. Rev. Microbiol.* **2017**, *71*, 643–664.

(14) Wang, W.; Du, Y.; Yang, S.; Du, X.; Li, M.; Lin, B.; Zhou, J.; Lin, L.; Song, Y.; Li, J.; Zuo, X.; Yang, C. Bacterial Extracellular Electron Transfer Occurs in Mammalian Gut. *Anal. Chem.* **2019**, *91*, 12138–12141.

(15) Schwab, L.; Rago, L.; Koch, C.; Harnisch, F. Identification of Clostridium cochlearium as an Electroactive Microorganism from the Mouse Gut Microbiome. *Bioelectrochemistry* **2019**, *130*, No. 107334.

(16) Khan, M. T.; Duncan, S. H.; Stams, A. J. M.; Van Dijl, J. M.; Flint, H. J.; Harmsen, H. J. M. The Gut Anaerobe Faecalibacterium prausnitzii Uses an Extracellular Electron Shuttle to Grow at Oxic–Anoxic Interphases. *ISME J.* **2012**, *6*, 1578–1585.

(17) Light, S. H.; Su, L.; Rivera-Lugo, R.; Cornejo, J. A.; Louie, A.; Iavarone, A. T.; Ajo-Franklin, C. M.; Portnoy, D. A. A Flavin-Based Extracellular Electron Transfer Mechanism in Diverse Gram-Positive Bacteria. *Nature* **2018**, *562*, 140–144.

(18) Bostick, C. D.; Mukhopadhyay, S.; Pecht, I.; Sheves, M.; Cahen, D.; Lederman, D. Protein Bioelectronics: A Review of What We Do and Do Not Know. *Rep. Prog. Phys.* **2018**, *81*, No. 026601.

(19) Wellman, S. M.; Eles, J. R.; Ludwig, K. A.; Seymour, J. P.; Michelson, N. J.; McFadden, W. E.; Vazquez, A. L.; Kozai, T. D. Y. A Materials Roadmap to Functional Neural Interface Design. *Adv. Funct. Mater.* **2018**, *28*, 1701269.

(20) Ha, T. Q.; Planje, I. J.; White, J. R. G.; Aragonès, A. C.; Díez-Pérez, I. Charge Transport at the Protein–Electrode Interface in the Emerging Field of BioMolecular Electronics. *Curr. Opin. Electrochem.* **2021**, *28*, No. 100734.

(21) Zhang, Y.; Hsu, L. H. H.; Jiang, X. Living Electronics. *Nano Res.* **2020**, *13*, 1205–1213.

(22) Sanjuan-Alberte, P.; Alexander, M. R.; Hague, R. J. M.; Rawson, F. J. Electrochemically Stimulating Developments in Bioelectronic Medicine. *Bioelectron. Med.* **2018**, *4*, 1–7.

(23) Sanjuan-Alberte, P.; Rawson, F. J. Engineering the Spark into Bioelectronic Medicine. *Ther. Delivery* **2019**, *10*, 139–142.

(24) Cohen-Karni, T.; Langer, R.; Kohane, D. S. The Smartest Materials: The Future of Nanoelectronics in Medicine. *ACS Nano* **2012**, *6*, 6541–6545.

(25) Alfonta, L. Bioelectrochemistry and the Singularity Point "I Robot"? *Isr. J. Chem.* **2021**, *61*, 60–67.

(26) Bird, L. J.; Kundu, B. B.; Tschirhart, T.; Corts, A. D.; Su, L.; Gralnick, J. A.; Ajo-Franklin, C. M.; Glaven, S. M. Engineering Wired Life: Synthetic Biology for Electroactive Bacteria. *ACS Synth. Biol.* **2021**, *10*, 2808–2823.

(27) Lovley, D. R. e-Biologics: Fabrication of Sustainable Electronics with "Green" Biological Materials. *MBio* **2017**, *8*, e00695-17.

(28) Lovley, D. R.; Yao, J. Intrinsically Conductive Microbial Nanowires for 'green' electronics with Novel Functions. *Trends Biotechnol.* **2021**, *39*, 940–952.

(29) Harnisch, F.; Holtmann, D.; *Bioelectrosynthesis*; Vol. *490*; Springer, 2019.

(30) Zou, L.; Zhu, F.; Long, Z. E.; Huang, Y. Bacterial Extracellular Electron Transfer: A Powerful Route to the Green Biosynthesis of Inorganic Nanomaterials for Multifunctional Applications. *J. Nanobiotechnol.* **2021**, *19*, 120.

(31) Sun, Y. L.; Tang, H. Y.; Ribbe, A.; Duzhko, V.; Woodard, T. L.; Ward, J. E.; Bai, Y.; Nevin, K. P.; Nonnenmann, S. S.; Russell, T.; Emrick, T.; Lovley, D. R. Conductive Composite Materials Fabricated from Microbially Produced Protein Nanowires. *Small* **2018**, *14*, No. e1802624.

(32) Gu, T.; Wang, D.; Lekbach, Y.; Xu, D. Extracellular Electron Transfer in Microbial Biocorrosion. *Curr. Opin. Electrochem.* **2021**, *29*, No. 100763.

(33) Kumar, A.; Hsu, L. H.-H.; Kavanagh, P.; Barrière, F.; Lens, P. N. L.; Lapinsonnière, L.; Lienhard V, J. H.; Schröder, U.; Jiang, X.; Leech, D. The Ins and Outs of Microorganism–Electrode Electron Transfer Reactions. *Nat. Rev. Chem.* **2017**, *1*, No. 0024.

(34) Baek, G.; Kim, J.; Kim, J.; Lee, C. Role and Potential of Direct Interspecies Electron Transfer in Anaerobic Digestion. *Energies* **2018**, *11*, 107.

(35) Karamash, M.; Stumpe, M.; Dengjel, J.; Salgueiro, C. A.; Giese, B.; Fromm, K. M. Reduction Kinetic of Water Soluble Metal Salts by Geobacter sulfurreducens: Fe2+/Hemes Stabilize and Regulate Electron Flux Rates. *Front. Microbiol.* **2022**, *13*, 2135.

(36) Reguera, G.; McCarthy, K. D.; Mehta, T.; Nicoll, J. S.; Tuominen, M. T.; Lovley, D. R. Extracellular Electron Transfer via Microbial Nanowires. *Nature* 2005, *435*, 1098−1101.

(37) Malvankar, N. S.; Vargas, M.; Nevin, K. P.; Franks, A. E.; Leang, C.; Kim, B. C.; Inoue, K.; Mester, T.; Covalla, S. F.; Johnson, J. P.; Rotello, V. M.; Tuominen, M. T.; Lovley, D. R. Tunable Metallic-Like Conductivity in Microbial Nanowire Networks. *Nat. Nanotechnol.* 2011, *6*, 573−579.

(38) Strycharz-Glaven, S. M.; Snider, R. M.; Guiseppi-Elie, A.; Tender, L. M. On the Electrical Conductivity of Microbial Nanowires and Biofilms. *Energy Environ. Sci.* 2011, *4*, 4366−4379.

(39) Malvankar, N. S.; Tuominen, M. T.; Lovley, D. R. Comment on "on Electrical Conductivity of Microbial Nanowires and Biofilms" by SM Strycharz-Glaven, RM Snider, A. Guiseppi-Elie and LM Tender, *Energy Environ. Sci.*, 2011, 4, 4366. *Energy Environ. Sci.* 2012, *5*, 6247−6249.

(40) Strycharz-Glaven, S. M.; Tender, L. M. Reply to the 'Comment on "On Electrical Conductivity of Microbial Nanowires and Biofilms"' by NS Malvankar, MT Tuominen and DR Lovley, *Energy Environ. Sci.*, 2012, 5, DOI: 10.1039/c2ee02613a. *Energy Environ. Sci.* 2012, *5*, 6250−6255.

(41) Yates, M. D.; Strycharz-Glaven, S. M.; Golden, J. P.; Roy, J.; Tsoi, S.; Erickson, J. S.; El-Naggar, M. Y.; Barton, S. C.; Tender, L. M. Measuring Conductivity of Living Geobacter sulfurreducens Biofilms. *Nat. Nanotechnol.* 2016, *11*, 910−913.

(42) Malvankar, N. S.; Rotello, V. M.; Tuominen, M. T.; Lovley, D. R. Reply To 'Measuring Conductivity of Living Geobacter sulfurreducens Biofilms'. *Nat. Nanotechnol.* 2016, *11*, 913−914.

(43) Nealson, K. H.; Myers, C. R. Microbial Reduction of Manganese and Iron: New Approaches to Carbon Cycling. *Appl. Environ. Microbiol.* 1992, *58*, 439−443.

(44) Reguera, G.; Kashefi, K. The Electrifying Physiology of Geobacter Bacteria, 30 Years On. *Adv. Microb. Physiol.* 2019, *74*, 1−96.

(45) Boesen, T.; Nielsen, L. P.; Schramm, A. Pili for Nanowires. *Nat. Microbiol.* 2021, *6*, 1347−1348.

(46) Wang, F.; Gu, Y.; O'Brien, J. P.; Yi, S. M.; Yalcin, S. E.; Srikanth, V.; Shen, C.; Vu, D.; Ing, N. L.; Hochbaum, A. I.; Egelman, E. H.; Malvankar, N. S. Structure of Microbial Nanowires Reveals Stacked Hemes That Transport Electrons over Micrometers. *Cell* 2019, *177*, 361−369.e10.

(47) Lovley, D. R.; Walker, D. J. F. Geobacter Protein Nanowires. *Front. Microbiol.* 2019, *10*, 2078.

(48) Yalcin, S. E.; Malvankar, N. S. The Blind Men and the Filament: Understanding Structures and Functions of Microbial Nanowires. *Curr. Opin. Chem. Biol.* 2020, *59*, 193−201.

(49) Lovley, D. R.; Holmes, D. E. Protein Nanowires: The Electrification of the Microbial World and Maybe Our Own. *J. Bacteriol.* 2020, *202*, No. e00331-20.

(50) Clark, M. M.; Reguera, G. Biology and Biotechnology of Microbial Pilus Nanowires. *J. Ind. Microbiol. Biotechnol.* 2020, *47*, 897−907.

(51) Gu, Y.; Srikanth, V.; Salazar-Morales, A. I.; Jain, R.; O'Brien, J. P.; Yi, S. M.; Soni, R. K.; Samatey, F. A.; Yalcin, S. E.; Malvankar, N. S. Structure of Geobacter Pili Reveals Secretory Rather than Nanowire Behaviour. *Nature* 2021, *597*, 430−434.

(52) Lovley, D. R. On the Existence of Pilin-Based Microbial Nanowires. *Front. Microbiol.* 2022, *13*, No. 872610.

(53) Ye, Y.; Liu, X.; Nealson, K. H.; Rensing, C.; Qin, S.; Zhou, S. Dissecting the Structural and Conductive Functions of Nanowires in Geobacter sulfurreducens Electroactive Biofilms. *MBio* 2022, *13*, No. e03822-21.

(54) Lovley, D. R. Untangling Geobacter sulfurreducens Nanowires. *MBio* 2022, *13*, No. e00850-22.

(55) Liu, X.; Nealson, K. H.; Zhou, S.; Rensing, C. Reply to Lovley, "Untangling *Geobacter Sulfurreducens* Nanowires.". *MBio* 2022, *13*, No. e01041-22.

(56) Yalcin, S. E.; O'Brien, J. P.; Gu, Y.; Reiss, K.; Yi, S. M.; Jain, R.; Srikanth, V.; Dahl, P. J.; Huynh, W.; Vu, D.; Acharya, A.; Chaudhuri, S.; Varga, T.; Batista, V. S.; Malvankar, N. S. Electric Field Stimulates Production of Highly Conductive Microbial OmcZ Nanowires. *Nat. Chem. Biol.* 2020, *16*, 1136−1142.

(57) Lovley, D. R. Electrically Conductive Pili: Biological Function and Potential Applications in Electronics. *Curr. Opin. Electrochem.* 2017, *4*, 190−198.

(58) Creasey, R. C. G.; Mostert, A. B.; Nguyen, T. A. H.; Virdis, B.; Freguia, S.; Laycock, B. Microbial Nanowires − Electron Transport and the Role of Synthetic Analogues. *Acta Biomater.* 2018, *69*, 1−30.

(59) Reardon, P. N.; Mueller, K. T. Structure of the Type IVa Major Pilin from the Electrically Conductive Bacterial Nanowires of Geobacter sulfurreducens. *J. Biol. Chem.* 2013, *288*, 29260−29266.

(60) Bonanni, P. S.; Massazza, D.; Busalmen, J. P. Stepping Stones in the Electron Transport from Cells to Electrodes in Geobacter sulfurreducens Biofilms. *Phys. Chem. Chem. Phys.* 2013, *15*, 10300−10306.

(61) Feliciano, G. T.; Steidl, R. J.; Reguera, G. Structural and Functional Insights into the Conductive Pili of Geobacter sulfurreducens Revealed in Molecular Dynamics Simulations. *Phys. Chem. Chem. Phys.* 2015, *17*, 22217−22226.

(62) Yan, H.; Chuang, C.; Zhugayevych, A.; Tretiak, S.; Dahlquist, F. W.; Bazan, G. C. Inter-aromatic Distances in Geobacter sulfurreducens Pili Relevant to Biofilm Charge Transport. *Adv. Mater.* 2015, *27*, 1908−1911.

(63) Xiao, K.; Malvankar, N. S.; Shu, C.; Martz, E.; Lovley, D. R.; Sun, X. Low Energy Atomic Models Suggesting a Pilus Structure That Could Account for Electrical Conductivity of Geobacter sulfurreducens Pili. *Sci. Rep.* 2016, *6*, 23385.

(64) Shu, C.; Xiao, K.; Sun, X. Structural Basis for the Influence of A1, 5A, and W51W57 Mutations on the Conductivity of the Geobacter sulfurreducens Pili. *Crystals* 2018, *8*, 10.

(65) Ru, X.; Zhang, P.; Beratan, D. N. Assessing Possible Mechanisms of Micrometer-Scale Electron Transfer in Heme-Free Geobacter sulfurreducens Pili. *J. Phys. Chem. B* 2019, *123*, 5035−5047.

(66) Shu, C.; Zhu, Q.; Xiao, K.; Hou, Y.; Ma, H.; Ma, J.; Sun, X. Direct Extracellular Electron Transfer of the Geobacter sulfurreducens Pili Relevant to Interaromatic Distances. *BioMed Res. Int.* 2019, *2019*, 6151587.

(67) Shu, C.; Xiao, K.; Sun, X. Structural Basis for the High Conductivity of Microbial Pili as Potential Nanowires. *J. Nanosci. Nanotechnol.* 2020, *20*, 64−80.

(68) Tan, Y.; Adhikari, R. Y.; Malvankar, N. S.; Ward, J. E.; Woodard, T. L.; Nevin, K. P.; Lovley, D. R. Expressing the Geobacter metallireducens PilA in Geobacter sulfurreducens Yields Pili with Exceptional Conductivity. *MBio* 2017, *8*, e02203-16.

(69) Mezzina Freitas, L. P.; Feliciano, G. T. Atomic and Electronic Structure of Pilus from Geobacter sulfurreducens through QM/MM Calculations: Evidence for Hole Transfer in Aromatic Residues. *J. Phys. Chem. B* 2021, *125*, 8305−8312.

(70) Amdursky, N.; Ferber, D.; Pecht, I.; Sheves, M.; Cahen, D. Redox Activity Distinguishes Solid-State Electron Transport from Solution-Based Electron Transfer in a Natural and Artificial Protein: Cytochrome C and Hemin-Doped Human Serum Albumin. *Phys. Chem. Chem. Phys.* 2013, *15*, 17142−17149.

(71) Agam, Y.; Nandi, R.; Kaushansky, A.; Peskin, U.; Amdursky, N. The Porphyrin Ring Rather Than the Metal Ion Dictates Long-Range Electron Transport across Proteins Suggesting Coherence-Assisted Mechanism. *Proc. Natl. Acad. Sci. U. S. A.* 2020, *117*, 32260−32266.

(72) Blumberger, J. Electron Transfer and Transport through Multi-heme Proteins: Recent Progress and Future Directions. *Curr. Opin. Chem. Biol.* 2018, *47*, 24−31.

(73) Futera, Z.; Ide, I.; Kayser, B.; Garg, K.; Jiang, X.; Van Wonderen, J. H.; Butt, J. N.; Ishii, H.; Pecht, I.; Sheves, M.; Cahen, D.; Blumberger, J. Coherent Electron Transport across a 3 nm Bioelectronic Junction Made of Multi-heme Proteins. *J. Phys. Chem. Lett.* 2020, *11*, 9766−9774.

(74) Boyd, D. A.; Snider, R. M.; Erickson, J. S.; Roy, J. N.; Strycharz-Glaven, S. M.; Tender, L. M. Theory of Redox Conduction and the

Measurement of Electron Transport Rates Through Electrochemically Active Biofilms. In *Biofilms in Bioelectrochemical Systems*; Beyenal, H.; Babauta, J. T., Eds.; Wiley, 2015; pp. 177−209.

(75) Page, C. C.; Moser, C. C.; Dutton, P. L. Mechanism for Electron Transfer Within and Between Proteins. *Curr. Opin. Chem. Biol.* **2003**, *7*, 551−556.

(76) Marcus, R. A. On the Theory of Oxidation-Reduction Reactions Involving Electron Transfer. I. *J. Chem. Phys.* **1956**, *24*, 966−978.

(77) Marcus, R. A. Discussion Comment on Mixed Reaction-Diffusion Controlled Rates. *Discuss. Faraday Soc.* **1960**, *29*, 21−31.

(78) Heitele, H. Dynamic Solvent Effects on Electron-Transfer Reactions. *Angew. Chem., Int. Ed. Engl.* **1993**, *32*, 359−377.

(79) Jiang, X.; van Wonderen, J. H.; Butt, J. N.; Edwards, M. J.; Clarke, T. A.; Blumberger, J. Which Multi-heme Protein Complex Transfers Electrons More Efficiently? Comparing MtrCAB from Shewanella with OmcS from Geobacter. *J. Phys. Chem. Lett.* **2020**, *11*, 9421−9425.

(80) Dahl, P. J.; Yi, S. M.; Gu, Y.; Acharya, A.; Shipps, C.; Neu, J.; O'Brien, J. P.; Morzan, U. N.; Chaudhuri, S.; Guberman-Pfeffer, M. J.; Vu, D.; Yalcin, S. E.; Batista, V. S.; Malvankar, N. S. A 300-Fold Conductivity Increase in Microbial Cytochrome Nanowires Due to Temperature-Induced Restructuring of Hydrogen Bonding Networks. *Sci. Adv.* **2022**, *8*, No. eabm7193.

(81) Eshel, Y.; Peskin, U.; Amdursky, N. Coherence-Assisted Electron Diffusion across the Multi-heme Protein-Based Bacterial Nanowire. *Nanotechnology* **2020**, *31*, 314002.

(82) Livernois, W.; Anantram, M.Quantum Transport in Conductive Bacterial Nanowires. In *16th Nanotechnology Materials and Devices Conference (NMDC)*; IEEE Publications, Vol. *2021*; 2021; pp. 1−5.

(83) Zheng, Z.; Gunner, M. R. Analysis of the Electrochemistry of Hemes with Ems Spanning 800 mV. *Proteins* **2009**, *75*, 719−734.

(84) Bertrand, P.; Mbarki, O.; Asso, M.; Blanchard, L.; Guerlesquin, F.; Tegoni, M. Control of the Redox Potential in c-Type Cytochromes: Importance of the Entropic Contribution. *Biochemistry* **1995**, *34*, 11071−11079.

(85) Verhagen, M. F. J. M.; Wolbert, R. B. G.; Hagen, W. R. Cytochrome c553 from Desulfovibrio vulgaris (Hildenborough) Electrochemical Properties and Electron Transfer with Hydrogenase. *Eur. J. Biochem.* **1994**, *221*, 821−829.

(86) Battistuzzi, G.; Bellei, M.; Borsari, M.; Di Rocco, G.; Ranieri, A.; Sola, M. Axial Ligation and Polypeptide Matrix Effects on the Reduction Potential of Heme Proteins Probed on Their Cyanide Adducts. *J. Biol. Inorg. Chem.* **2005**, *10*, 643−651.

(87) Larroque, C.; Maurel, P.; Douzou, P. Redox Potentials in Hydro-organic Media at Normal and Subzero Temperatures Ferro-Ferricyanide and Cytochrome c as Models. *Biochim. Biophys. Acta* **1978**, *501*, 20−32.

(88) Anderson, C. W.; Halsall, H. B.; Heineman, W. R.; Kreishman, G. P. The Temperature Dependence of the Redox Potential of Horse Heart Cytochrome c in Sodium Chloride Solutions. *Biochem. Biophys. Res. Commun.* **1977**, *76*, 339−344.

(89) Battistuzzi, G.; Borsari, M.; Cowan, J. A.; Ranieri, A.; Sola, M. Control of Cytochrome c Redox Potential: Axial Ligation and Protein Environment Effects. *J. Am. Chem. Soc.* **2002**, *124*, 5315−5324.

(90) Reid, L. S.; Taniguchi, V. T.; Gray, H. B.; Mauk, A. G. Oxidation-Reduction Equilibrium of Cytochrome b5. *J. Am. Chem. Soc.* **1982**, *104*, 7516−7519.

(91) Battistuzzi, G.; Borsari, M.; Ranieri, A.; Sola, M. Redox Thermodynamics of the Fe3+/Fe2+ Couple in Horseradish Peroxidase and Its Cyanide Complex. *J. Am. Chem. Soc.* **2002**, *124*, 26−27.

(92) Wang, F.; Mustafa, K.; Suciu, V.; Joshi, K.; Chan, C. H.; Choi, S.; Su, Z.; Si, D.; Hochbaum, A. I.; Egelman, E. H.; Bond, D. R. Cryo-EM Structure of an Extracellular Geobacter OmcE Cytochrome Filament Reveals Tetrahaem Packing. *Nat. Microbiol.* **2022**, *7*, 1291−1300.

(93) Wang, F.; Chan, C. H.; Suciu, V.; Mustafa, K.; Ammend, M.; Si, D.; Hochbaum, A. I.; Egelman, E. H.; Bond, D. R. Structure of Geobacter OmcZ Filaments Suggests Extracellular Cytochrome Polymers Evolved Independently Multiple Times. *Elife* **2022**, *11*, No. e81551.

(94) Breuer, M.; Rosso, K. M.; Blumberger, J. Electron Flow in Multiheme Bacterial Cytochromes Is a Balancing Act between Heme Electronic Interaction and Redox Potentials. *Proc. Natl. Acad. Sci. U. S. A.* **2014**, *111*, 611−616.

(95) Bradshaw, R. T.; Dziedzic, J.; Skylaris, C. K.; Essex, J. W. The Role of Electrostatics in Enzymes: Do Biomolecular Force Fields Reflect Protein Electric Fields? *J. Chem. Inf. Model.* **2020**, *60*, 3131−3144.

(96) Cruzeiro, V. W. D.; Feliciano, G. T.; Roitberg, A. E. Exploring Coupled Redox and pH Processes with a Force-Field-Based Approach: Applications to Five Different Systems. *J. Am. Chem. Soc.* **2020**, *142*, 3823−3835.

(97) O'Donoghue, D.; Magner, E. The Redox Thermodynamics of Microperoxidase are Dependent on the Solvent Medium. *Chem. Commun.* **2003**, *3*, 438−439.

(98) Knapp, M. J.; Rickert, K.; Klinman, J. P. Temperature-Dependent Isotope Effects in Soybean Lipoxygenase-1: Correlating Hydrogen Tunneling with Protein Dynamics. *J. Am. Chem. Soc.* **2002**, *124*, 3865−3874.

(99) Huynh, M. H. V.; Meyer, T. J. Colossal Kinetic Isotope Effects in Proton-Coupled Electron Transfer. *Proc. Natl. Acad. Sci.* **2004**, *101*, 13138−13141.

(100) Tyburski, R.; Liu, T.; Glover, S. D.; Hammarström, L. Proton-coupled Electron Transfer Guidelines, Fair and Square. *J. Am. Chem. Soc.* **2021**, *143*, 560−576.

(101) Zahler, C. T.; Shaw, B. F. What Are We Missing by Not Measuring the Net Charge of Proteins? *Chemistry* **2019**, *25*, 7581−7590.

(102) Amdursky, N.; Pecht, I.; Sheves, M.; Cahen, D. Electron Transport via Cytochrome C on Si−H Surfaces: Roles of Fe and Heme. *J. Am. Chem. Soc.* **2013**, *135*, 6300−6306.

(103) Jiang, X.; Futera, Z.; Ali, M. E.; Gajdos, F.; von Rudorff, G. F.; Carof, A.; Breuer, M.; Blumberger, J. Cysteine Linkages Accelerate Electron Flow through Tetra-Heme Protein STC. *J. Am. Chem. Soc.* **2017**, *139*, 17237−17240.

(104) Filman, D. J.; Marino, S. F.; Ward, J. E.; Yang, L.; Mester, Z.; Bullitt, E.; Lovley, D. R.; Strauss, M. Cryo-EM Reveals the Structural Basis of Long-Range Electron Transport in a Cytochrome-Based Bacterial Nanowire. *Commun. Biol.* **2019**, *2*, 219.

(105) Ru, X.*Nanometer to Micrometer Electron Transfer: Incoherent Hopping in Biomolecular Systems*; Duke University, 2020.

(106) Bortolotti, C. A.; Siwko, M. E.; Castellini, E.; Ranieri, A.; Sola, M.; Corni, S. The Reorganization Energy in Cytochrome C is Controlled by the Accessibility of the Heme to the Solvent. *J. Phys. Chem. Lett.* **2011**, *2*, 1761−1765.

(107) Tipmanee, V.; Oberhofer, H.; Park, M.; Kim, K. S.; Blumberger, J. Prediction of Reorganization Free Energies for Biological Electron Transfer: A Comparative Study of Ru-Modified Cytochromes and a 4-Helix Bundle Protein. *J. Am. Chem. Soc.* **2010**, *132*, 17032−17040.

(108) Ghosh, C.; Kara, A.; Rahman, T. S. Usage of Pattern Recognition Scheme in Kinetic Monte Carlo Simulations: Application to Cluster Diffusion on Cu(1 1 1). *Surf. Sci.* **2007**, *601*, 3159−3168.

(109) Leetmaa, M.; Skorodumova, N. V. Mean Square Displacements with Error Estimates from Non-equidistant Time-Step Kinetic Monte Carlo Simulations. *Comput. Phys. Commun.* **2015**, *191*, 119−124.

(110) Nenashev, A. V.; Jansson, F.; Baranovskii, S. D.; Österbacka, R.; Dvurechenskii, A. V.; Gebhard, F. Effect of Electric Field on Diffusion in Disordered Materials. I. One-Dimensional Hopping Transport. *Phys. Rev. B* **2010**, *81*, No. 115203.

(111) Jansson, F.*Charge Transport in Disordered Materials: Simulations, Theory, and Numerical Modeling of Hopping Transport and Electron-Hole Recombination*; Ph.D. Dissertation, Åbo Akademi University, Turku, Finland, 2011.

(112) Ing, N. L.; El-Naggar, M. Y.; Hochbaum, A. I. Going the Distance: Long-Range Conductivity in Protein and Peptide Bioelectronic Materials. *J. Phys. Chem. B* **2018**, *122*, 10403−10423.

(113) Phan, H.; Yates, M. D.; Kirchhofer, N. D.; Bazan, G. C.; Tender, L. M.; Nguyen, T.-Q. Biofilm as a Redox Conductor: A Systematic Study of the Moisture and Temperature Dependence of Its Electrical Properties. *Phys. Chem. Chem. Phys.* **2016**, *18*, 17815−17821.

(114) Roy, S.; Xie, O.; Dorval Courchesne, N. M. Challenges in Engineering Conductive Protein Fibres: Disentangling the Knowledge. *Can. J. Chem. Eng.* **2020**, *98*, 2081−2095.

(115) Ing, N. L.; Nusca, T. D.; Hochbaum, A. I. Geobacter sulfurreducens Pili Support Ohmic Electronic Conduction in Aqueous Solution. *Phys. Chem. Chem. Phys.* **2017**, *19*, 21791−21799.

(116) Yates, M. D.; Golden, J. P.; Roy, J.; Strycharz-Glaven, S. M.; Tsoi, S.; Erickson, J. S.; El-Naggar, M. Y.; Barton, S. C.; Tender, L. M. Thermally Activated Long Range Electron Transport in Living Biofilms. *Phys. Chem. Chem. Phys.* **2015**, *17*, 32564−32570.

(117) Bellissent-Funel, M.-C.; Hassanali, A.; Havenith, M.; Henchman, R.; Pohl, P.; Sterpone, F.; Van Der Spoel, D.; Xu, Y.; Garcia, A. E. Water Determines the Structure and Dynamics of Proteins. *Chem. Rev.* **2016**, *116*, 7673−7697.

(118) Mejía, L.; Kleinekathöfer, U.; Franco, I. Coherent and Incoherent Contributions to Molecular Electron Transport. *J. Chem. Phys.* **2022**, *156*, No. 094302.

(119) Marcus, R. A.; Sutin, N. The Relation between the Barriers for Thermal and Optical Electron Transfer Reactions in Solution. *Comments Inorg. Chem.* **1986**, *5*, 119−133.

(120) Marcus, R. A.; Sutin, N. Electron-Transfer Reactions with Unusual Activation Parameters. Treatment of Reactions Accompanied by Large Entropy Decreases. *Inorg. Chem.* **1975**, *14*, 213−216.

(121) Braddock, J. N.; Meyer, T. J. Kinetics of the Oxidation of Hexaaquoiron (2+) by Polypyridine Complexes of Ruthenium (III). Negative Enthalpies of Activation. *J. Am. Chem. Soc.* **1973**, *95*, 3158−3162.

(122) Cramer, J. L.; Meyer, T. J. Unusual Activation Parameters in the Oxidation of Hexaaquairon (2+) Ion by Polypyridine Complexes of Iron (III). Evidence for Multiple Paths for Outer-Sphere Electron Transfer. *Inorg. Chem.* **1974**, *13*, 1250−1252.

(123) Kirmaier, C.; Holten, D.; Parson, W. W. Temperature and Detection-Wavelength Dependence of the Picosecond Electron-Transfer Kinetics Measured in Rhodopseudomonas sphaeroides Reaction Centers. Resolution of New Spectral and Kinetic Components in the Primary Charge-Separation Process. *Biochim. Biophys. Acta, Bioenerg.* **1985**, *810*, 33−48.

(124) Fleming, G. R.; Martin, J. L.; Breton, J. Rates of Primary Electron Transfer in Photosynthetic Reaction Centres and Their Mechanistic Implications. *Nature* **1988**, *333*, 190−192.

(125) Shuai, Z.; Geng, H.; Xu, W.; Liao, Y.; André, J. M. From Charge Transport Parameters to Charge Mobility in Organic Semiconductors through Multiscale Simulation. *Chem. Soc. Rev.* **2014**, *43*, 2662−2679.

(126) Matyushov, D. V. Dynamical Effects in Protein Electrochemistry. *J. Phys. Chem. B* **2019**, *123*, 7290−7301.

(127) Coutinho, N. D.; Silva, V. H. C.; de Oliveira, H. C. B.; Camargo, A. J.; Mundim, K. C.; Aquilanti, V. Stereodynamical Origin of Anti-Arrhenius Kinetics: Negative Activation Energy and Roaming for a Four-Atom Reaction. *J. Phys. Chem. Lett.* **2015**, *6*, 1553−1558.

(128) Coutinho, N. D.; Aquilanti, V.; Silva, V. H. C.; Camargo, A. J.; Mundim, K. C.; de Oliveira, H. C. B. Stereodirectional Origin of Anti-Arrhenius Kinetics for a Tetraatomic Hydrogen Exchange Reaction: Born−Oppenheimer Molecular Dynamics for OH+ HBr. *J. Phys. Chem. A* **2016**, *120*, 5408−5417.

(129) Waskasi, M. M.; Kodis, G.; Moore, A. L.; Moore, T. A.; Gust, D.; Matyushov, D. V. Marcus Bell-Shaped Electron Transfer Kinetics Observed in an Arrhenius Plot. *J. Am. Chem. Soc.* **2016**, *138*, 9251−9257.

(130) Waskasi, M. M.; Newton, M. D.; Matyushov, D. V. Impact of Temperature and Non-gaussian Statistics on Electron Transfer in Donor−Bridge−Acceptor Molecules. *J. Phys. Chem. B* **2017**, *121*, 2665−2676.

(131) Matyushov, D. V. Energetics of Electron-Transfer Reactions in Soft Condensed Media. *Acc. Chem. Res.* **2007**, *40*, 294−301.

(132) Kirchberg, H.; Thorwart, M.; Nitzan, A. Charge Transfer through Redox Molecular Junctions in Nonequilibrated Solvents. *J. Phys. Chem. Lett.* **2020**, *11*, 1729−1737.

(133) Gangopadhyay, D.; Ganguly, B. N.; Mukherjee, T.; Dutta-Roy, B. Anti-Arrhenius Behaviour in Positronium Chemistry: A Kramers' Turnover? *Chem. Phys. Lett.* **2000**, *318*, 161−167.

(134) Kramers, H. A. Brownian Motion in a Field of Force and the Diffusion Model of Chemical Reactions. *Physica* **1940**, *7*, 284−304.

(135) Matyushov, D. V. Non-ergodic Electron Transfer in Mixed-Valence Charge-Transfer Complexes. *J. Phys. Chem. Lett.* **2012**, *3*, 1644−1648.

(136) Sarhangi, S. M.; Matyushov, D. V. Anomalously Small Reorganization Energy of the Half Redox Reaction of Azurin. *J. Phys. Chem. B* **2022**, *126*, 3000−3011.

(137) Waskasi, M. M.; Martin, D. R.; Matyushov, D. V. Wetting of the Protein Active Site Leads to Non-Marcusian Reaction Kinetics. *J. Phys. Chem. B* **2018**, *122*, 10490−10495.

(138) Sowa, J. K.; Marcus, R. A. On the Theory of Charge Transport and Entropic Effects in Solvated Molecular Junctions. *J. Chem. Phys.* **2021**, *154*, No. 034110.

(139) Benderskii, V. A.; Goldanskii, V. I.; Makarov, D. E. Quantum Dynamics in Low-Temperature Chemistry. *Phys. Rep.* **1993**, *233*, 195−339.

(140) Meisner, J.; Kästner, J. Atom Tunneling in Chemistry. *Angew. Chem., Int. Ed. Engl.* **2016**, *55*, 5400−5413.

(141) Dewar, M. J.; Merz, K. M.; Stewart, J. J. Vibrationally Assisted Tunnelling (VAT) in a 1, 5 Hydrogen Shift? *J. Chem. Soc., Chem. Commun.* **1985**, *3*, 166−168.

(142) Carvalho-Silva, V. H.; Coutinho, N. D.; Aquilanti, V. Description of Deviations from Arrhenius Behavior in Chemical Kinetics and Materials Science. In *AIP Conference Proceedings*; AIP Publishing LLC2016,*1790* (1), 020006, DOI: 10.1063/1.4968632

(143) Murakami, K.; Tanaka, Y.; Sakai, R.; Hisai, Y.; Hayashi, S.; Mizutani, Y.; Higo, T.; Ogo, S.; Seo, J. G.; Tsuneki, H.; Sekine, Y. Key Factor for the Anti-Arrhenius Low-Temperature Heterogeneous Catalysis Induced by H^+ Migration: H^+ Coverage Over Support. *Chem. Commun.* **2020**, *56*, 3365−3368.

(144) de la Lande, A.; Cailliez, F.; Salahub, D. R.Electron Transfer Reactions in Enzymes: Seven Things That Might Break down in Vanilla Marcus Theory and How to Fix Them If They Do. In *Simulating Enzyme Reactivity: Computational Methods in Enzyme Catalysis*; Moliner, V.; Tunon, I., Eds.; Royal Society of Chemistry, 2016; pp. 89−149.